Exploiting Hydrophone Flow Noise Spatiotemporal Correlation for Enhanced Signal Detection

Final Report

Prepared by Garth Frazier

and

Wayne Prather

National Center for Physical Acoustics

University of Mississippi

29 April 2022

Synopsis

Flow noise pressure fluctuations created by wall-bounded turbulence is a common problem limiting the performance of underwater hydrophone systems. Its effects are often reduced by one or methods including using a large array with a large number of hydrophones and beamforming processing, increasing the effective size of the pressure sensing diaphragm of each sensor element to create local noise averaging, by using a small compact array of hydrophones and direct averaging (possibly with different weights) for local noise averaging, or by reducing the speed the hydrophones are moved through the water. Of course, a combination of these techniques is also useful.

It is demonstrated in this document that significantly more processing gain can achieved with the compact array idea if more sophisticated processing is performed than just simple or weighted averaging. The reason this can be achieved is the fact that flow noise can be well correlated (coherent) on short spatiotemporal scales and thus appears almost like a plane wave to the compact array. This document presents the mathematical development of how to exploit this property of flow noise in applications where the acoustic signals are statistically stationary and demonstrates through analysis and simulation potential processing gains. While not developed in this document, similar results are achievable in applications involving transient acoustic events and active sonar.

Moreover, results from an experiment performed using a compact array of eight flush-mounted patch hydrophones towed underwater in a nearby freshwater lake are presented and analyzed. While the experiment did not proceed as originally planned, the results nevertheless qualitatively demonstrate that using the proposed processing method with a compact array provides performance gains over simple averaging of the measurements to suppress flow noise.

We note that similar ideas have been developed and by the U.S. Navy in the past [1, 2] but the idea proposed here significantly extends them to more sensors and more sophisticated signal processing.

The goal

The goal of the following investigation is to demonstrate the feasibility of using compact hydrophone arrays (described below) to enable significant processing gain against flow noise (wall-bounded pressure fluctuations) by exploiting its potentially high coherence on short spatiotemporal scales.

The compact array hypothesis

Let there be a very small array consisting of N_c sensor elements such that the greatest inter-sensor spacing is much shorter (perhaps as much as two orders of magnitude) than the shortest acoustic wavelength of interest. Thus, it is reasonable to assume the acoustic component of the all the measurements is essentially the same on all of the elements at the same time instant. Assume that the inter-sensor spacing is such that, as an array, the shortest wavelength of the noise process does not exhibit significant spatial aliasing and that the temporal sampling rate satisfies the Shannon sampling theorem. Also assume that the flow noise process is additive and is independent from all acoustic processes. We shall refer to this set of assumptions as the *compact array hypothesis*.

Array of compact arrays model

Assume there is a standard sensor array consisting of N_a compact arrays as elements and that each compact array consists of N_c elements. Furthermore, assume that all acoustic sources are sufficiently distant from the array so that plane wave approximations are valid. Thus, the total acoustic signal measured at the centroid of the compact array k is

$$y_{s_k}^m(i\omega) = \sum_{j=1}^{N_s} y_{s_j}(i\omega) exp\left(-i\omega r_k^T w_j\right) \in C, \quad (1)$$

where $N_s < N_a$ is the number of acoustic signals, the $y_{s_j}(i\omega) \in C$ are the individual acoustic signals at the standard array's reference location, the $w_j \in R^3$ are the corresponding acoustic slowness vectors, and $r_k \in R$ is the position vector of the centroid of compact array k with relative to the array's reference frame. Also, assume that the acoustic sources are mutually statistically independent. The total signal plus noise measurement at array k is

$$y_k^m(i\omega) = a y_{s_k}^m(i\omega) + y_{n_k}^m(i\omega) \in C^{N_c}, \quad (2)$$

where $a \in R^{N_c}$ is a vector of all ones (this is application of the compact array hypothesis). At each compact array denote the complex covariance *matrix* for the measured data (acoustic signals plus non-acoustic noise) as

$$S_{y^m}(\omega) = \sigma_s^2(\omega) a a^T + S_n(\omega), \quad (3)$$

where $\sigma_s^2(\omega) \in R$ is the average power density of the *sum* of the all the independent acoustic signals, and $S_n(\omega)$ is the flow noise cross-spectral density matrix *where it has been assumed that the noise process has the same statistics at each array*. Also, note that $\sigma_s^2(\omega)$ is the same value for all compact arrays under the plane waves and statistically independent acoustic signals assumptions. Of course, this value is not known in advance. Then the minimum mean-squared error (MMSE) estimate of the *total* acoustic signal at compact array k is

$$\hat{y}_{s_k}(i\omega) = \sigma_s^2(\omega) a^T S_{y^m}^{-1}(\omega) y_k^m(i\omega). \quad (4)$$

For compact arrays (see the next section), the power spectral density of the flow noise is assumed to be of the form

$$S_n(\omega) = \sigma_n^2(\omega) C_n(\omega), \quad (5)$$

where $\sigma_n^2(\omega)$ is the flow noise power spectral density, and $C_n(\omega)$ is a complex coherence matrix with ones on the diagonal. Using this assumption and the well-known result for the MMSE estimation error

$$\sigma_e^2(\omega) = [\sigma_n^{-2}(\omega) a^T C_n^{-1}(\omega) a + \sigma_s^{-2}]^{-1}, \quad (6)$$

it can be shown that the compact array output $SNR_{mmse}^{out}(\omega) = \sigma_s^2(\omega)/\sigma_e^2(\omega)$ is

$$SNR_{mmse}^{out}(\omega) = 1 + SNR^{in}(\omega)a^T C_n^{-1}(\omega)a. \quad (7)$$

So, it is clear that all other quantities being fixed, the coherence structure of the flow noise is the governing factor influencing performance of a compact array. Not surprisingly, in the case the flow noise is incoherent ($C_n^{-1}(\omega) = I$), the nominal array gain factor of N_c is recovered. However, it is apparent that gain factors less than or greater than N_c are also possible.

Of course, the total signal power density $\sigma_s^2(\omega)$ is not known in advance. However, define the estimator

$$\hat{y}_{s_k}(i\omega) = \frac{\hat{y}_{s_k}(i\omega)}{\sigma_s^2(\omega)a^T S_{y^m}^{-1}(\omega)a} = \frac{a^T S_{y^m}^{-1}(\omega)y_k^m(i\omega)}{a^T S_{y^m}^{-1}(\omega)a}, \quad (8)$$

which is simply the MMSE estimate scaled by a real number and can be calculated directly from the data. Expanding (8) yields

$$\hat{y}_{s_k}(i\omega) = y_{s_k}^m(i\omega) + \frac{a^T S_{y^m}^{-1}(\omega)}{a^T S_{y^m}^{-1}(\omega)a} y_{n_k}^m(i\omega), \quad (9)$$

which reveals the partition of the true signal component and noise component contributions to the signal estimate. Using the Sherman-Morrison matrix identity it can be shown that the error power in this estimator is

$$\sigma_e^2(\omega) = \frac{\sigma_n^2(\omega)}{a^T C_n^{-1}(\omega)a}, \quad (10)$$

which is always greater than the MMSE estimator and is statistically equivalent to the Generalized Least-Squares (GLS) estimator. Furthermore, in terms of SNR,

$$SNR_{gls}^{out}(\omega) = SNR^{in}(\omega)a^T C_n^{-1}(\omega)a, \quad (11)$$

which indicates a simple expression for the compact array gain. Since the factor $a^T C_n^{-1}(\omega)a$ appears in the performance indicators for both estimators, it will be referred to as the *compact array gain factor*,

$$G(\omega) = a^T C_n^{-1}(\omega)a. \quad (12)$$

The error powers of these estimators can misleading indicators for array processing (beamforming) since they assess distance in the complex plane only and not phase error explicitly: Two points in the complex plane can arbitrarily close while the phase error can be as much as pi radians. For if phase error is the concern, then it is obvious that larger signal power will reduce average phase error for a fixed noise power, but this is not indicated in previous equations for error power. Therefore, relative error with respect to the signal (inverse of SNR) is proposed as a more suitable measure of performance. For MMSE the relative error is

$$\sigma_{r_{mmse}}^2(\omega) = \frac{1}{1 + SNR^{in}G(\omega)}, \quad (13)$$

and for the GLS processor

$$\sigma^2_{r_{gls}}(\omega) = \frac{1}{SNR^{in}G(\omega)}. \quad (14)$$

It is worthwhile to note that under the compact array hypothesis it is possible to estimate the total signal average power density using information contained in (3) since every entry in $S_{y^m}(\omega)$ has the form

$$S_{y^m}(\omega)_{mn} = \sigma^2_s(\omega) + \sigma^2_n(\omega)\gamma^2_{mn}(\omega)exp(-i\omega r^T_{mn}v), \quad (15)$$

where r_{mn} is a relative position vector of two elements of the compact array, $\gamma^2_{mn}(\omega)$ is the coherence squared, and v is the flow noise pressure fluctuation convection velocity vector (see the next section). Since $S_{y^m}(\omega)_{mn}$ can be estimated from the data, a *flow* noise model fitting error term J_{mn} can be written in terms of parameters v and $\sigma^2_s(\omega)$ as

$$J_{mn} = exp(-i\omega r^T_{mn}v) - \frac{S_{y^m}(\omega)_{mn} - \sigma^2_s(\omega)}{\left|S_{y^m}(\omega)_{mn} - \sigma^2_s(\omega)\right|}, \quad (16)$$

which eliminates the need to estimate $\sigma^2_n(\omega)\gamma^2_{mn}(\omega)$. This is essentially a measure of the phase error (notice the normalization after removal of the acoustic power term) of the flow noise model with respect to the data. Since this equation can be written for all entries of $S_{y^m}(\omega)$ there will be sufficient information to obtain a unique solution for v and $\sigma^2_s(\omega)$ upon suitable minimization of the fitting errors. *Therefore, using the resulting estimate for $\sigma^2_s(\omega)$ it is possible to approach the performance of the MMSE estimator which is superior to the GLS estimator without knowing the signal power in advance.* The cost is the extra (non-linear) processing.

In any case, using the compact array output $\hat{y}_{s_k}(i\omega)$ (Equation 4) or $\hat{y}_{s_k}(i\omega)$ (Equation 8) from each compact array, it is straightforward to form a cross-spectral density matrix for the overall array system and estimate the signals' slowness vectors using a standard beamforming technique. To simulate the performance of this idea, a model for the cross-spectrum of the flow noise is required, and this is presented in the following section.

A model for the cross-spectrum of flow noise

In order to simulate the above processing strategy, we use the model presented in [3] (with slightly modified notation) for the flow noise. The form of the cross-spectral density is

$$R(\zeta, \eta, \omega) = \frac{R^*(\omega)e^{-i\frac{\omega}{U_c}\zeta}\alpha^3}{\left[\alpha^2 + m^2\left(\frac{\eta}{\delta}\right)^2 + \left(\frac{\zeta}{\delta}\right)^2\right]^{\frac{3}{2}}}, \quad (17)$$

where $R^*(\omega)$ is the auto-spectral density, U_c is the frequency dependent *convection velocity of pressure*, ζ is the separation distance along the direction of flow, η is the separation distance transverse to the flow, α is an empirical decay coefficient given by

$$\alpha(\omega,\delta,u_\tau)=\frac{4.7}{\pi}\frac{1}{\sqrt{1+3\times10^{-5}\left(\frac{\omega}{\delta u_\tau}-50\right)^2}}, \tag{18}$$

u_τ is the friction velocity, δ is the boundary layer thickness, and $m\approx 7.7$ is an empirical scaling factor. If we consider compact arrays consisting of a 1D array along the direction of flow, then η is zero. Therefore, high coherence of the flow noise is achieved when the ratio of the sensor spacing to the boundary layer thickness much less than α. Notice that α is a decreasing function of frequency, but is an increasing function of the product of the boundary layer thickness and the friction velocity. Thus a thicker boundary layer improves coherence, but so does greater shear stress. Unfortunately, greater shear stress creates greater pressure fluctuations as seen below.

For the auto-spectral density the form suggested in [4] and used in [3] is

$$R^*(\omega)=\frac{3\tau_w^2\left(\frac{\omega\delta}{U_e}\right)^3}{\left[\left(\frac{\omega\delta}{U_e}\right)^{0.75}+0.5\right]^{3.7}+\left[\left(1.1R_T^{-0.57}\right)\left(\frac{\omega\delta}{U_e}\right)\right]^7}, \tag{19}$$

where τ_w is shear stress at the wall, U_e is the flow velocity at the edge of the boundary layer, and R_T is a ratio of time scales where

$$R_T=\left(\frac{u_\tau}{U_e}\right)\left(\frac{u_\tau\delta}{\nu}\right), \tag{20}$$

and ν is the kinematic viscosity. Reference [5] demonstrates that the model from [4], while originally formulated for air, is effective for underwater applications. Reference [5] also gives $U_c=\left[0.6+exp\left(-0.87\frac{\omega\delta}{U_e}\right)\right]U_e$ for the pressure fluctuation convection speed.

Analysis results

Assume a compact array consisting of ten sensor elements arranged according to Figure 1. Logarithmic spacing has been utilized in order to provide more consistent performance across a range of flow speeds than achievable with an evenly spaced array. Also assume that the sensors are free from electronic noise *and that they measure pressure at a single point*. Real hydrophones will always have a finite measurement area, and this will reduce the flow noise level in the measurements via the effect of spatial averaging. Using the models described above, compact array gain factors were calculated for theoretical best performance (upper bound) of the as a function of the following three parameters: flow speed, Reynolds number, and acoustic frequency. Figure 2, Figure 3, and Figure 4 present results corresponding to increasing Reynolds number. While all of the conditions show gain, it is obvious that the higher Reynolds numbers produce much better performance, higher flow speeds degrade performance, and there is a peak performance frequency given that the other two parameters are fixed.

It is important to understand how *absolute* flow noise levels change as a function of these parameters as well. Figure 5, Figure 6, Figure 7 present the power spectral density of the flow noise model corresponding to increasing Reynolds number. While the general trend is for higher levels of noise with increasing Reynolds number, this is not entirely true as the 2 m/s curves indicate. Recall that increasing Reynolds number leads to better compact array gain factor, thus higher gains achieved under higher Reynolds number are somewhat offset by the higher noise levels. Of course, there is usually very little that can be done to change the Reynolds numbers of the flow environment without significant design changes that control the fluid-structure interaction. Therefore, the higher gain factors corresponding to higher Reynolds numbers are of significant practical importance.

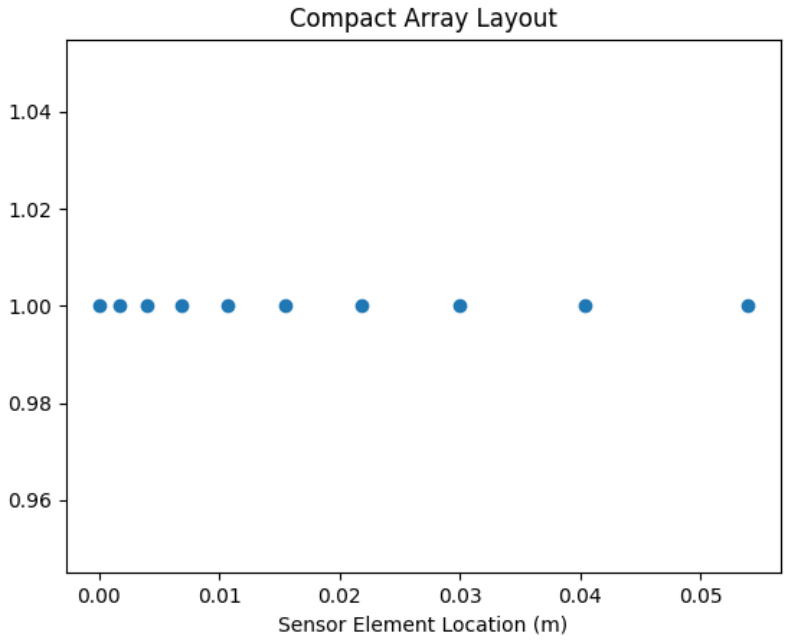

Figure 1. 1D Compact array layout showing logarithmic spacing

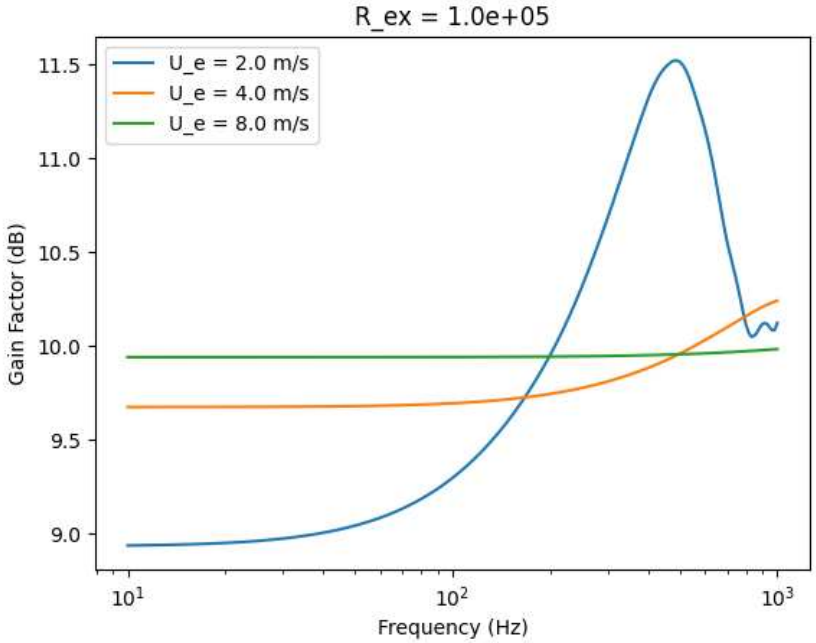

Figure 2. Compact array gain factor for Reynolds number $R_{ex} = 1 \times 10^5$. The ordinate scale has little variation over the frequency range from 10 to 1000 Hz; however, at the lowest flow rate of 2 m/s a peak gain of 11.5 dB is achieved.

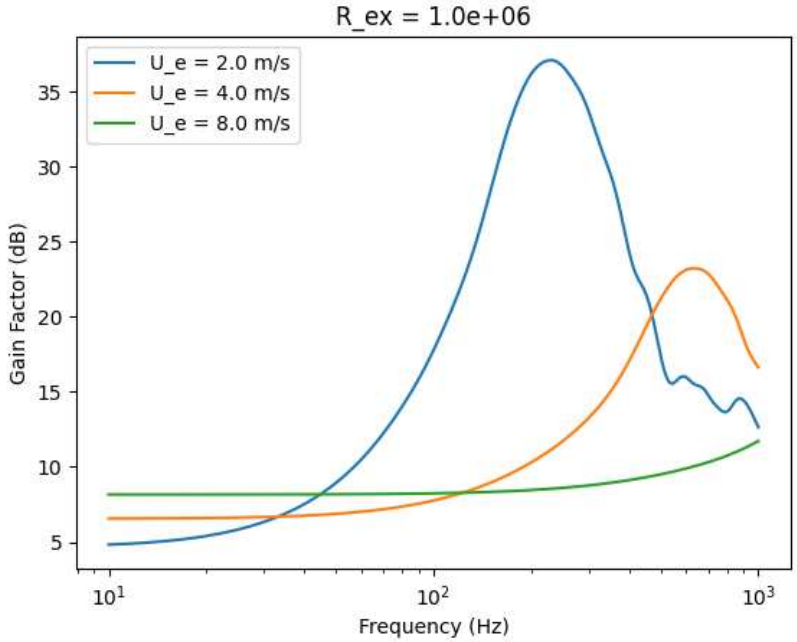

Figure 3. Compact array gain factor for Reynolds number $R_{ex} = 1 \times 10^6$ reveals a significant improvement over $R_{ex} = 1 \times 10^5$; however, at the highest flow rate of 8 m/s little gain is achieved.

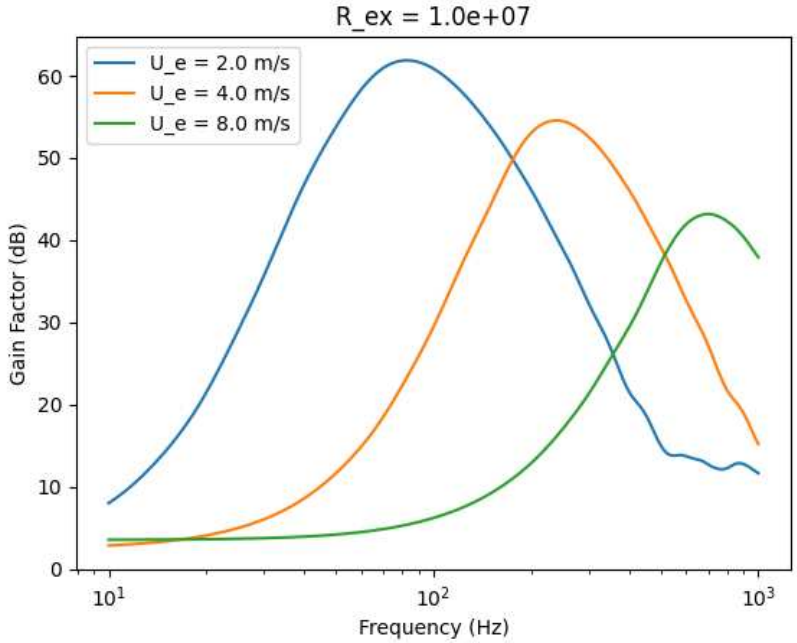

Figure 4. Compact array gain factor for Reynolds number $R_{ex} = 1 \times 10^7$ reveals substantial performance gains even at low frequencies for 2 m/s flow speeds.

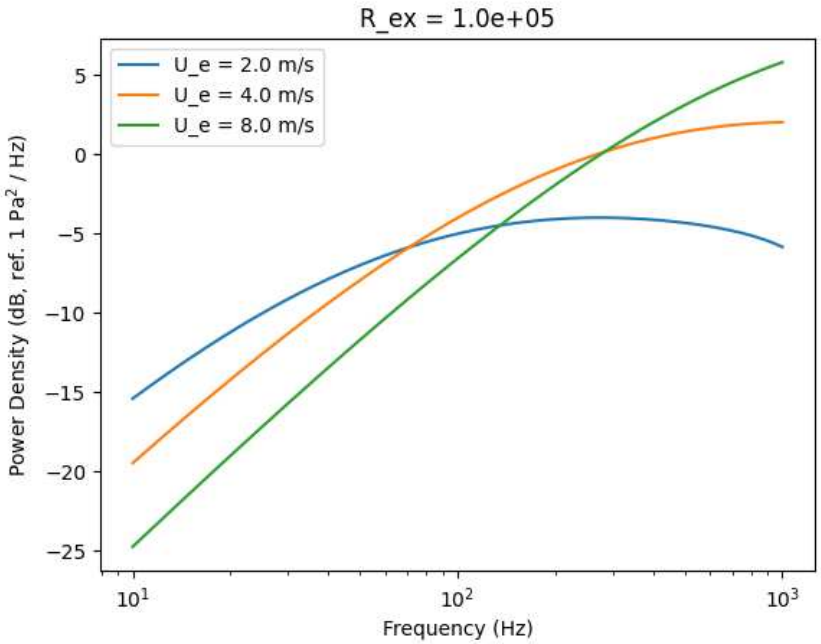

Figure 5. Flow noise corresponding to Reynolds number $R_{ex} = 1 \times 10^5$. Notice that it is generally an increasing function of frequency.

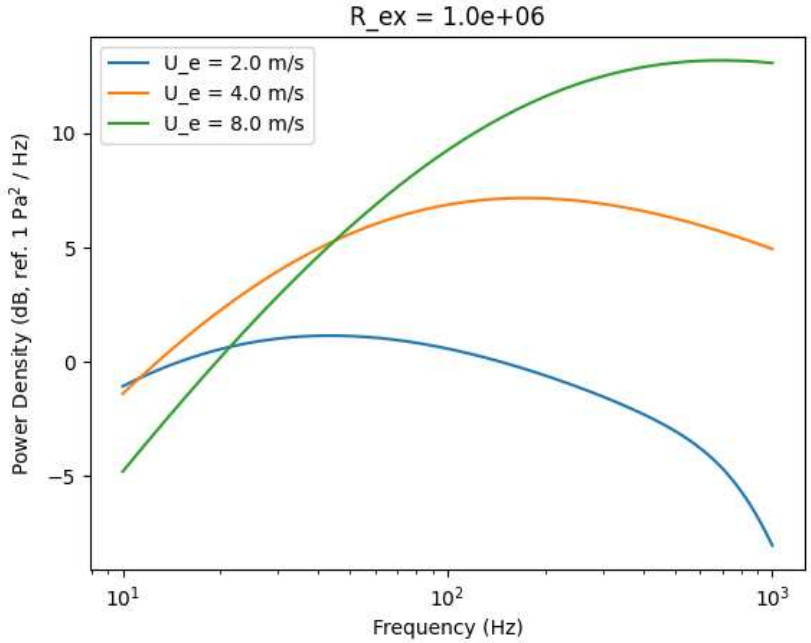

Figure 6. Flow noise corresponding to Reynolds number $R_{ex} = 1 \times 10^6$. Not only is the noise much greater than for a lower Reynolds number, but the shapes of the curves differ significantly as a function of flow speed.

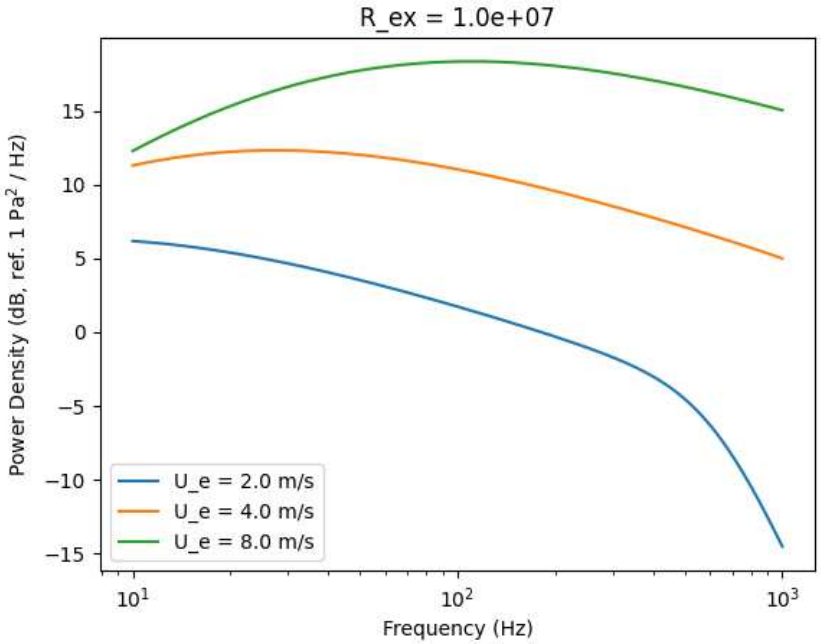

Figure 7. Flow noise corresponding to Reynolds number $R_{ex} = 1 \times 10^7$. Here the curves for the two highest flow rates do not vary substantially as a function of frequency, but for the slowest flow rate power density drops off significantly as a function of frequency.

Simulation results

In order to demonstrate that a system designed around using compact arrays can substantially outperform a system based on individual sensing elements, a Monte Carlo simulation of a generic array system was performed. The layout of the simulated array system is provided in Figure 8. Each location consists of a compact array as described in the previous section. The results do not correspond to any particular realistic system, but are intended only to demonstrate the potential performance gains associated with using compact arrays in a flow noise environment when multiple sources are present in a single frequency bin. Standard MUSIC was used as the array processor under the assumption of two sources (the correct number), and 50 simulations were run to obtain statistics. Figure 9, Figure 10, and Figure 11 are a sampling of simulation results. The captions provide discussion of the individual cases, but the general result, based on a review of all the results, indicates, not unexpectedly, that the compact array system is consistently superior to single sensor systems. Nevertheless, there were some unexpected results based on the compact array factor analysis of the previous section. Often, low Reynolds number cases produce very good results even though the compact array gain factor was less than high Reynolds number cases.

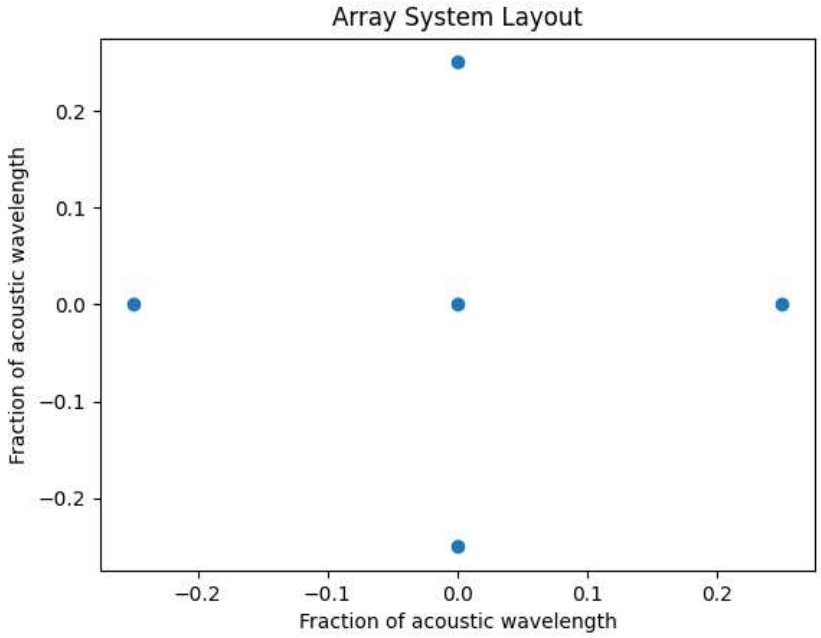

Figure 8. Array system layout used for Monte Carlo simulation. Since each simulation was performed on a single frequency bin, the inter-sensor spacing was adjusted according to the acoustic wavelength in order to maintain a consistent performance comparison. Fluid flow is assumed to be from left to right in all simulations.

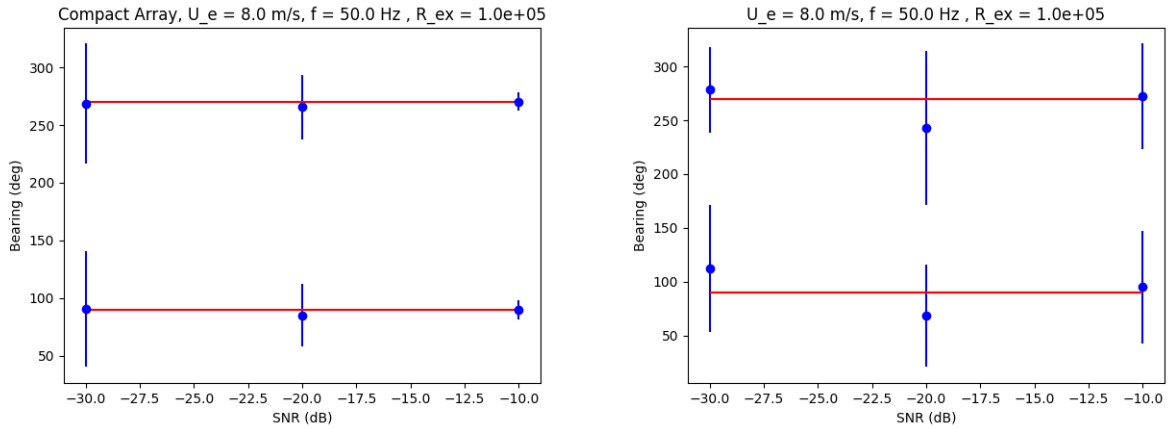

Figure 9. Simulation results corresponding to flow rate 8 m/s, frequency 50 Hz, and Reynolds number 1×10^5. On the left are compact array system results, on the right the single sensor system results. The red lines indicate the correct bearings, and the blue indicators correspond to the simulations. Error bars are one standard deviation. At -20 dB SNR bias occurs in both cases, but at -10 dB SNR, the compact array system shows significantly superior performance in terms of standard deviation.

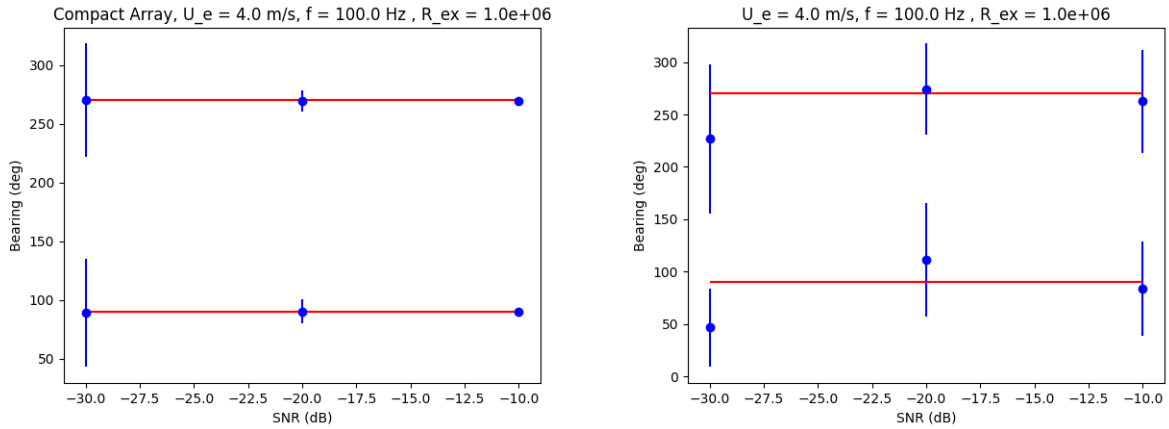

Figure 10. Simulation results corresponding to flow rate 4 m/s, frequency 100 Hz, and Reynolds number 1×10^6. On the left are compact array system results, on the right the single sensor system results. The red lines indicate the correct bearings, and the blue indicators correspond to the simulations. Error bars are one standard deviation. In all cases the compact array system is clearly superior.

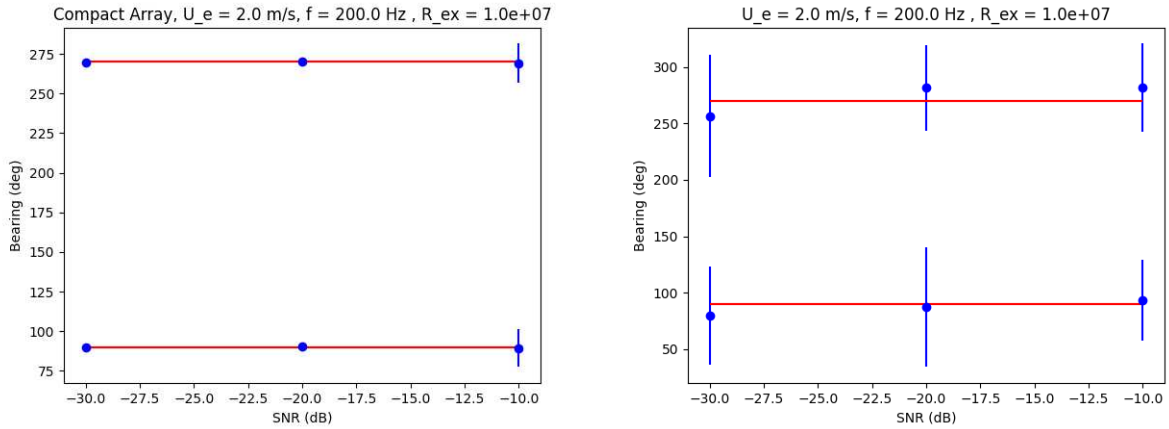

Figure 11. Simulation results corresponding to flow rate 2 m/s, frequency 200 Hz, and Reynolds number 1×10^7. On the left are compact array system results, on the right the single sensor system results. The red lines indicate the correct bearings, and the blue indicators correspond to the simulations. Error bars are one standard deviation. Again, the compact array system demonstrates superior performance. Interestingly, the performance degraded at the highest SNR in terms of standard deviation. This warrants further investigation.

Cross-spectral density between two finite patch hydrophones

In order to simulate realistic (finite pressure sensing area) hydrophones the cross-spectral density function between a pair of them must be derived in terms of patch geometry and the flow noise two-point cross-spectral density function. Suppose two hydrophones correspond to 2D shapes defined by sets S_1 and S_2 with respect to a fixed coordinate frame. Assume that the measured force $f_m(t)$ on each is defined as

$$f_m(t) = \int_{S_m} p(x_m, y_m|, t) dS_m, m = 1,2, \tag{21}$$

where $p(x_m, y_m, t)$ is the pressure at point $(x_m, y_m) \in S_m$ created by a wind-sense (at least) stationary (WSS) random process. Then, by definition, the cross-correlation function is

$$R_{12}(\tau) = E[f_1(t) f_2(t + \tau)], \tag{22}$$

where $E[\cdot]$ is the expectation operator. Upon substitution,

$$R_{12}(\tau) = E \tag{23}$$

or

$$R_{12}(\tau) = \int_{S_1} \int_{S_2} E[p(x_1, y_1, t) p(x_2, y_2, t + \tau)] dS_1 dS_2, \tag{24}$$

which leads to

$$R_{12}(\tau) = \int_{S_1} \int_{S_2} R_p(x_1, x_2, y_1, y_2, \tau) dS_1 dS_2, \tag{25}$$

for the WSS assumption where R_p is the flow noise cross-correlation function. Fourier transforming the temporal variable results in the desired cross-spectral density function

$$Q_{12}(\omega) = \int_{S_1} \int_{S_2} Q_p(x_1, x_2, y_1, y_2, \omega) dS_1 dS_2, \tag{26}$$

where Q_p is the two-point cross-spectral density of the flow noise.

Compact array gain estimates using finite area patch elements

It is well known that finite area patch arrays provide significant gain against flow noise [6]. Even more gain has been achieved when compact arrays have been used where the outputs of each patch are weighted (array shading) with fixed values [7]. Using the cross-spectral density function $Q_{12}(\omega)$ from above, the compact array gain factor of compact arrays constructed with surface-mounted, finite area patch elements can estimated and compared with the gain achievable using just a single patch array having the same area as all of the compact array patch elements combined.

In the first case a single 20-by-20 mm patch was analyzed. Breaking this into eight elements along the direction of flow produces a compact array of equal area with each element being 20-by-5/2 mm. An equivalent approach for compact arrays of 40-by-40 mm and 80-by-80 mm all utilizing 8 elements. The following figures present the performance comparison results. To perform the required integration for each patch a simplistic rectangular rule was used for the 2-D iterated integrals.

Analysis of the figures reveals that compact array performance is equal to or superior to a single patch of equal total surface area. This should not be surprising because the compact array has more information to work with, so to speak. For the cases analyzed the best performance appears to correspond to a Reynolds number of 1e7 and a flow speed of 5 m/s. While higher Reynolds numbers correspond to higher noise levels, even if only slightly, the thicker turbulent boundary layer associated with the higher number appears to produce better results. While not shown here, this is because the turbulent fluid remains more stable as it flows across the surface.

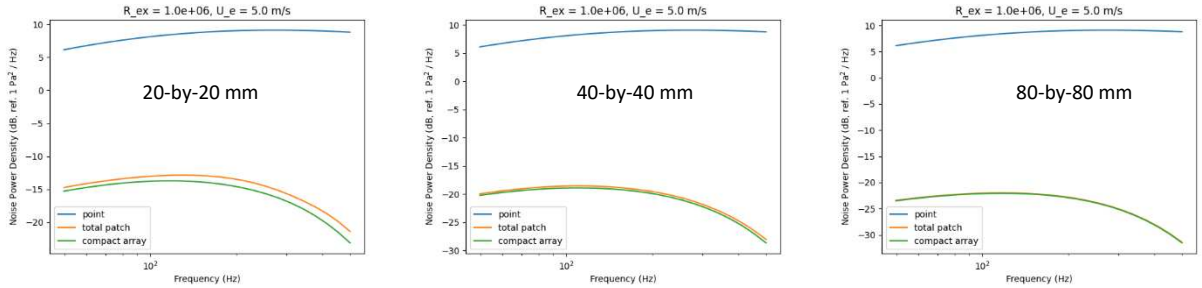

Figure 12. Noise performance comparison for Reynold's Number 1e6 and flow speed of 5 m/s for 20-by-20 mm, 40-by-40 mm, and 80-by-80 mm (left to right) patch arrays. Each figure has a plot of the noise

power density at a point, the output of a single patch and the output of an 8-element compact patch array of total size equal to the single patch. In this case, the compact array does not offer any advantages.

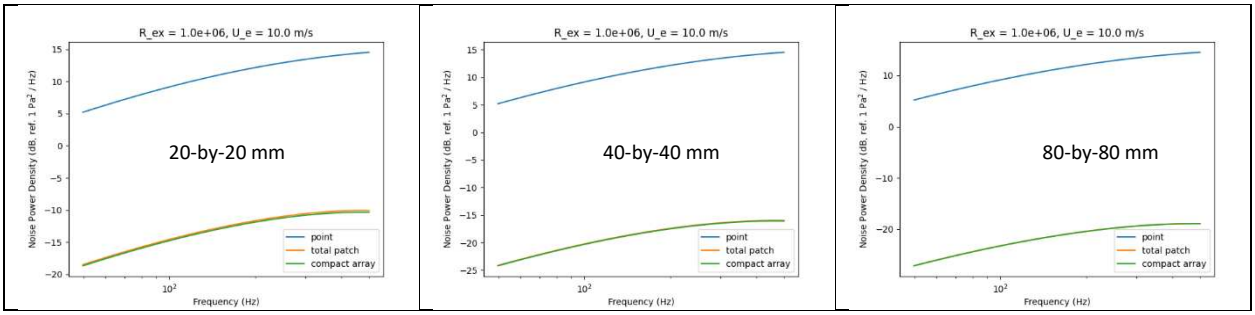

Figure 13. Same as Figure 12, but for higher flow rate of 10 m/s. Again, the compact array offers no advantage over a single patch.

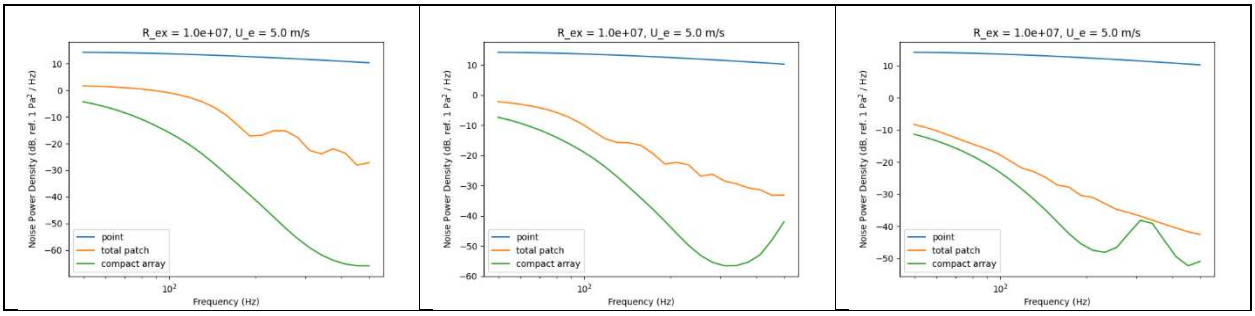

Figure 14. Same as Figure 12, but for higher Reynold's Number of 1e7 (more developed turbulence). Now the advantage of the compact array becomes apparent. Note that while the flow noise is greater than in Figure 12, the performances of the single patch and compact array are better in absolute terms.

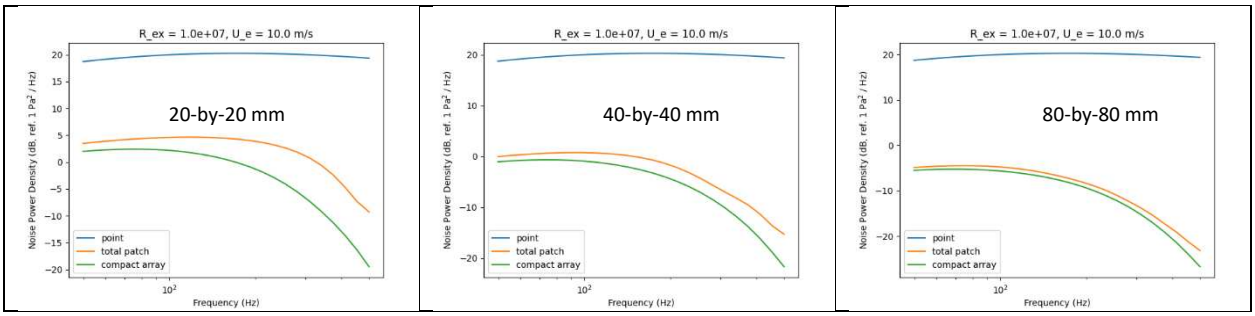

Figure 15. Same as Figure 15. Same as, but for higher flow rate of 10 m/s. Again performance of the compact array is better that just the simple patch of the same total area.

Improving the evaluation of integrals for finite patch array elements

In the previous section compact array performance results corresponding to finite-area patch array elements were calculated using simplistic, iterated rectangular rule integration. While this is

straightforward to implement, it is computationally intense if accurate results are to be obtained. We investigated trying to improve this situation by performing analytical analysis of the relevant integrals.

Essentially we need to integrate

$$\iint_D R\ \ (\omega)\, e^{\frac{-i\omega}{U_c}\zeta} \frac{\alpha^3}{\left[\alpha^2 + \left(\frac{\eta}{\delta m}\right)^2 + \left(\frac{\zeta}{\delta}\right)^2\right]^{\frac{3}{2}}} d\zeta d\eta, \tag{27}$$

where the domain $D = \{\zeta \in [\zeta_1, \zeta_2], \eta \in [\eta_1, \eta_2]\}$.

Firstly, by Fubini's Theorem rewrite the integral above as an iterated integral

$$\alpha^3 R\ \ (\omega) \int_{\zeta_1}^{\zeta_2} e^{\frac{-i\omega}{U_c}\zeta} \int_{\eta_1}^{\eta_2} \frac{1}{\left[\alpha^2 + \left(\frac{\eta}{\delta m}\right)^2 + \left(\frac{\zeta}{\delta}\right)^2\right]^{\frac{3}{2}}} d\eta d\zeta. \tag{28}$$

Now it is possible to focus on the inner integral

$$I(\zeta) = \int_{\eta_1}^{\eta_2} \frac{1}{\left[\alpha^2 + \left(\frac{\eta}{\delta m}\right)^2 + \left(\frac{\zeta}{\delta}\right)^2\right]^{\frac{3}{2}}} d\eta, \tag{29}$$

which can be written as

$$\delta m \int_{x_1}^{x_2} \frac{1}{[\mu^2 + x^2]^{\frac{3}{2}}} dx, \tag{30}$$

where $\mu^2 = \alpha^2 + \left(\frac{\zeta}{\delta}\right)^2$, and $x = \frac{\eta}{\delta m}$. Making the additional substitution $x = \mu tan\theta$ leads to

$$\frac{\delta m}{\mu^2} \int_{\theta_1}^{\theta_2} cos\theta\, dx = \frac{\delta m}{\mu^2} [sin\theta_2 - sin\theta_1]. \tag{31}$$

After substitution of the previous changes of variables the final form becomes

k
$$I(\zeta) = \frac{\eta_2}{\left(\alpha^2 + \left(\frac{\zeta}{\delta}\right)^2\right)\sqrt{\alpha^2 + \left(\frac{\zeta}{\delta}\right)^2 + \left(\frac{\eta_2}{\delta m}\right)^2}} - \frac{\eta_1}{\left(\alpha^2 + \left(\frac{\zeta}{\delta}\right)^2\right)\sqrt{\alpha^2 + \left(\frac{\zeta}{\delta}\right)^2 + \left(\frac{\eta_1}{\delta m}\right)^2}}. \tag{32}$$

Now it is only necessary to use a 1-D quadrature scheme to evaluate

$$\alpha^3 R(\omega) \int_{\zeta_1}^{\zeta_2} e^{\frac{-i\omega}{U_c}\zeta} I(\zeta) d\zeta. \tag{33}$$

While we have not implemented this into the compact array performance analysis software, a quick check on few examples reveals almost an order of magnitude reduction in computation times.

Optimal detection and estimation of transients

The previously presented results correspond to estimation of stationary signals in noise. In many applications, the goal is to detect a transient waveform of relatively short duration—a pulse from an echo, for example. The processing in this case is performed most naturally in the time domain. The simplest way to develop an optimal processing strategy is using operator notation. Assume that the flow noise (or all of the background noise including acoustic clutter) measured on the N_c channels of a compact array is modeled as a multivariate, finite-order, linear, time-invariant (LTI) random process operator P, and that the transient acoustic waveform is modeled as the impulse response of single-input, single-output linear, LTI system operator T. Furthermore, assume that the compact array hypothesis applies. Then we know that the operator T that minimizes the GLS (vector) error equation

$$\epsilon = P^{-1}\big[y - aT[u]\big], \tag{34}$$

where y is a finite duration measured compact array data vector that can be written as

$$y = y_p + y_t = y_p + aT[u]; \tag{35}$$

where y_p is the background noise, and y_t is the acoustic transient; a is a vector of ones; u is a discrete-time Dirac delta function; characterizes the transient acoustic waveform estimate. The role of the operator P^{-1} is to whiten the natural error just as the weighting matrix does in finite-dimensional GLS estimation. Of course, the work is to develop a computational strategy to find T to minimize the objective function

$$J = \frac{1}{2}\epsilon^T\epsilon. \tag{36}$$

Note that

$$E[\epsilon\epsilon^T] = P^{-1}E\big[y_p y_p^T\big]P^{-T}, \tag{37}$$

so if $E\big[y_p y_p^T\big]$ can be written in terms of operator P such that $E\big[y_p y_p^T\big] = PP^T$, then

$$E[\epsilon\epsilon^T] = I, \tag{38}$$

the identity operator. This implies that ϵ is a white noise process with identity covariance matrix.

Firstly, assume that P is parameterized as a final equations form vector, autoregressive, moving-average random (VARMA) process, i.e.,

$$y_p(k) = \sum_{i=1}^{N_p} a_i y_p(k-i) + \sum_{j=1}^{N_p} B_j w(k-j) + w(k), \tag{39}$$

where w is a zero-mean white noise process with nonsingular covariance matrix Ω_p. Final equations form implies each a_i is a scalar, and the B_j are square matrices. This enforces identifiability (a unique representation). Then it is clear that the sequence

$$w(k) = y_p(k) - \sum_{i=1}^{N_p} a_i y_p(k-i) - \sum_{j=1}^{N_p} B_j w(k-j), \tag{40}$$

defines an operator such that if $\Omega_p = B_0 B_0^T$,

$$E[B_0^{-1} w(k) w^T(k) B_0^{-T}] = I, \tag{41}$$

where I in this case is the identity matrix. So if the VARMA coefficients and the covariance matrix Ω_p can be estimated prior to the arrival of the transient, then the operator P^{-1} is available.

Now parameterize the transient acoustic operator T as a ARX process

$$y_t(k) = \sum_{i=1}^{N_t} c_i y_t(k-i) + \sum_{j=1}^{N_t} d_j u(k-j), \tag{42}$$

where $u(k) = I(k - k_0)$ for some k_0, where I is the discrete-time Direc delta. Given the ARX coefficients $\{c_i\}$, $\{d_j\}$, and a start time k_0, the sequence $\{y_t\}$ can be generated. Applying the operator equation (34) generates the error sequence from which the objective function J can be calculated. By systematically adjusting the ARX coefficients and possibly the start time to minimize J, the optimal estimate for the transient waveform can be obtained.

To summarize, the proposed algorithm for estimating a transient acoustic waveform with a compact array is presented below.

1. Specify a starting dynamical orders for the background process (flow noise plus stationary acoustic signals) and the acoustic transient.
2. Using the continuously measured time series from the all the channels of a compact array and a recursive algorithm continuously update the VARMA coefficients, including the dynamical order, for the operator P.
3. Using an anomaly detector, continuously monitor the prediction error of the VARMA estimation algorithm for a potential acoustic transient. This includes an estimate of its start time and duration.
4. Upon transient detection, estimate the ARX coefficients, including the dynamical order, for the operator T using the compact array measurements determined by the detector that are assumed to include a transient. Do not update the parameters of the operator P with these measurements. This can be accomplished using nonlinear multivariate optimization. Analytical expressions for the gradient of J can be obtained using vibrational calculus.
5. Starting with the measurements immediately following the transient, return to step 2.

Turbulence Induced Noise Reduction Field Test

Purpose

The purpose of the field test was to collect data from a compact array of hydrophones mounted on an underwater flat surface with dimensions that are large enough to allow for the formation of a developed

turbulent boundary layer at the location of the hydrophones. The theoretical development discussed in section 1 suggests that using closely spaced array elements along with appropriate signal processing techniques allows for increased noise reduction beyond that which is possible with standard averaging. The field test was designed to test these conclusions in real world conditions and compare the actual noise reduction gain achieved to the theoretical expected gain.

Experimental Design

The general concept of the testing is that this 'fin' is towed behind a boat at different speeds to create a range of flow speeds. The range of flow speeds of interest are from 1 to 10 m/s. Based on these goals and the intersection of practicality it was decided that the fin upon which the hydrophones are mounted has facial dimensions of 1.0 meters in depth and 0.5 meters in height and the thickness of 0.0381 meters (1.5 inches). This gives a Reynolds number of 0.38 x 10^6 for flow at 1 m/s and 3.8 x 10^6 for flow at 10 m/sec which suggest the presence of a developed turbulent boundary layer for all flow speeds at the location of the sensors. In this design the hydrophones are mounted linearly in the flow as far back from the leading edge as practical and vertically in the middle of the fin. The chosen hydrophones are TE Connectivity Measurement Specialties FLDT1-028K PVDF Piezo film-based sensors. The partially assembled design can be seen in Figure 16 with the eight rectangular piezo plates in the rear center being the hydrophone sensors. The distance from the leading edge of the fin to the center of the first sensor is 0.8m. The sensing area of each hydrophone is 12 mm by 30 mm with a PVDF film thickness of 28 µm and a 15.75 mm center-to-center spacing of the eight elements. In operation the fin travels through the water vertically with flow going from left to right for the orientation shown in the figure. The finished fin with a 1.25 mm layer of urethane rubber potting material (Smooth-On VytaFlex 60) covering the sensors is shown in Figure 17. The basic hydrodynamic profile of the fin can be seen in Figure 18.

The theory suggest that the effectiveness of the proposed technique is a function of the boundary layer thickness, and it increases as the boundary layer thickness increases. In order to maximize the boundary layer thickness at the location of the sensors a roughened turbulence trip strip was added directly behind the leading edge of the hydro foil. This strip was constructed by gluing larger sized sand particles in a 5 cm wide strip from top to bottom as seen in Figure 19. As discussed later in more detail this was only done on one side of the fin.

Various methods were conceived for how to drag the fin through the water at the range of flow speeds of interest with the final decision being made to tow a kayak with the fin mounted underneath behind a boat. One important concept in the design was the need to minimize any coupling of mechanical vibrations from the kayak through the mounting structure into the fin. This is due to the very sensitive nature of the piezo hydrophones to picking up structure borne vibrational energy in the fin. The fear was that vibrational energy in the kayak due to it being physically towed or its interaction with the roughness of the surface of the water would couple into the fin through the mount and cause significant noise in the measurements. In order to combat this the fin mounting structure was designed such that the mounting pole from the fin plugs into a PVC pipe structurally mounted to the kayak. The PVC pipe was completely lined on the inside with foam padding material such that full rotation and limited vertical freedom of motion for the fin could occur while never allowing it to come into direct contact with the structure of the kayak. The general concept of this in operation can be seen in Figure 20 and Figure 21. Additional 3D printed blue hydro foil shrouds can be seen in Figure 21 which were designed to cover the mounting pole to minimize drag and eliminate the possibility of any issues due to Von Karman vortex shedding interacting

with the sensors. Power and data cables are brought up through the mounting pole of the fin into the kayak and installed to the data collection computer. The data collection computer is contained in the yellow pelican case strapped to the kayak as seen in Figure 20 and Figure 21. The process of installing the fin can be seen in Figure 21.

In order to assess the measured noise reduction as a signal to noise ratio (SNR) improvement, the original intent was to have two acoustic sources playing at specific times each of the following signals; 50 Hz tone, 100 Hz tone, 200 Hz tone, 400 Hz tone, 800 Hz tone, white noise band pass filtered from 50 Hz to 1 kHz, and a series of impulsive pops. The acoustic sources consisted of an ElectroVoice UW30 underwater speakers. An acoustic source in close proximity to the fin during operation was obtained by installing the EV UW30 speaker in a 'body board' which was towed closely behind the kayak and powered by an audio amplifier housed on the kayak. This setup can be seen in Figure 22. A second source at larger distances was designed to be lowered to the floor of the lake from a second boat anchored off the shore. This second source was to remain stationary as the boat towed the fin by it with closest point of approach distances expected to be in the 100 – 500 meter range. The depth of the stationary source below the water was designed to be between 3 – 10 meters. While operational and ready to be deployed the stationary source was not employed due to issues with the kayak/fin system to be described further down in the report.

The data collection system contained in the fin consisted of a Measurement Computing USB-1808X 8 channel simultaneous sampling ADC with a sample rate of 200 kSPS/ch. A custom preamplifier board was designed and assembled to interface the eight piezo hydrophones to the USB-1808X board. As discussed earlier, power and USB cables were routed to this board through the interior of the fin and its mounting pole. These components were mounted in a pocket machined in the fin behind the aluminum cover plate seen in Figure 16. The rest of the data collection components consisting of a Raspberry Pi 4 single board computer and a Garmin 18 LX GPS receiver were mounted in the yellow Pelican case as seen in Figure 20. A wireless serial radio was also connected to the Raspberry Pi 4 computer to allow remote access and control of the data collection system. In addition to the data collection equipment an audio amplifier was installed in the yellow Pelican box for driving the towed audio source. Power for the data collection system was supplied by a 22 Volt LiPo battery and power for the audio amplifier was supplied by a 12 Volt marine deep cycle lead acid battery. Connection through the wireless radio link also allowed for control of the audio source and what sound files were played through the source. Instantaneous time and location information were saved with the acoustic data utilizing the system clock on the computer and the Garmin GPS device.

Test Matrix

- Tow the fin through the water at the following four speeds;
  - 0 m/s.
  - 2.5 m/s.
  - 5 m/s.
  - 10 m/sec.
- At each of these four speeds collect data for at least 30 seconds while playing each of the following signals through the acoustic source;
  - 50 Hz Tone
  - 100 Hz Tone

  - 200 Hz Tone
  - 400 Hz Tone
  - 800 Hz Tone
  - White noise band filtered between 50 Hz and 1 kHz
  - Series of impulsive pops
- Perform this series of runs once with the towed source active and the repeat it with the remote source active at a closest point of approach of approximately 100 m.

Experimental Results / Issues

Due to an unforeseen issue the test did not go as planned and all of the desired data was not obtained. Fortunately, data was obtained for all signals played by the towed source at speeds of 0 m/sec. and as high as 1 m/s. but flow speeds greater than this were not obtainable. Due to tunnel vision focus on the turbulent boundary layer thickness over the sensors, there was a critical oversight in failing to add an equivalent 'turbulence trip strip' on the back side of the fin to insure symmetric flow over both sides. Because the flow over the fin was not symmetric the fin had to have an 'angle of attack' before the hydrodynamic forces balanced. When towed this 'angle of attack' caused the direction of travel of the fin to not align with the direction of tow thus having a perpendicular as well as in line component to its path as towed. Because of the relative size of the fin as compared to the kayak this imposed a significant lateral force on the kayak as it moved forward. Due to their shape kayaks have very little lateral stability and as such was quickly overwhelmed at speeds greater than 1 m/s. As stated above, data was taken at speeds up to the point at which the kayak became unacceptable unstable.

Additional issues also plagued this test in that although waterproof MDF panel board was purchased and used it turned out to not be as waterproof as described. Extensive additional efforts were made to ensure that the fin was as watertight as possible by both sealing any gaps or holes and painting it multiple times with waterproof urethane. Unfortunately, anywhere the board became exposed to water the board swelled which then cause more exposure and a larger scale degradation. These issues prevented any further testing in the time allowed.

It is worth noting that lessons learned and further contemplation revealed a much simpler and more trustworthy way to accomplish the desired testing at the desired speeds which eliminates the need for the kayak and allows for towing the fin directly. Given that the results from this test show very promising results and agreement with the theory it is our strong desire to somehow make a second attempt at measurements over the entire flow speed range using the improved fin design.

Figure 16- Partially finished fin showing 8 piezo hydrophone sensors

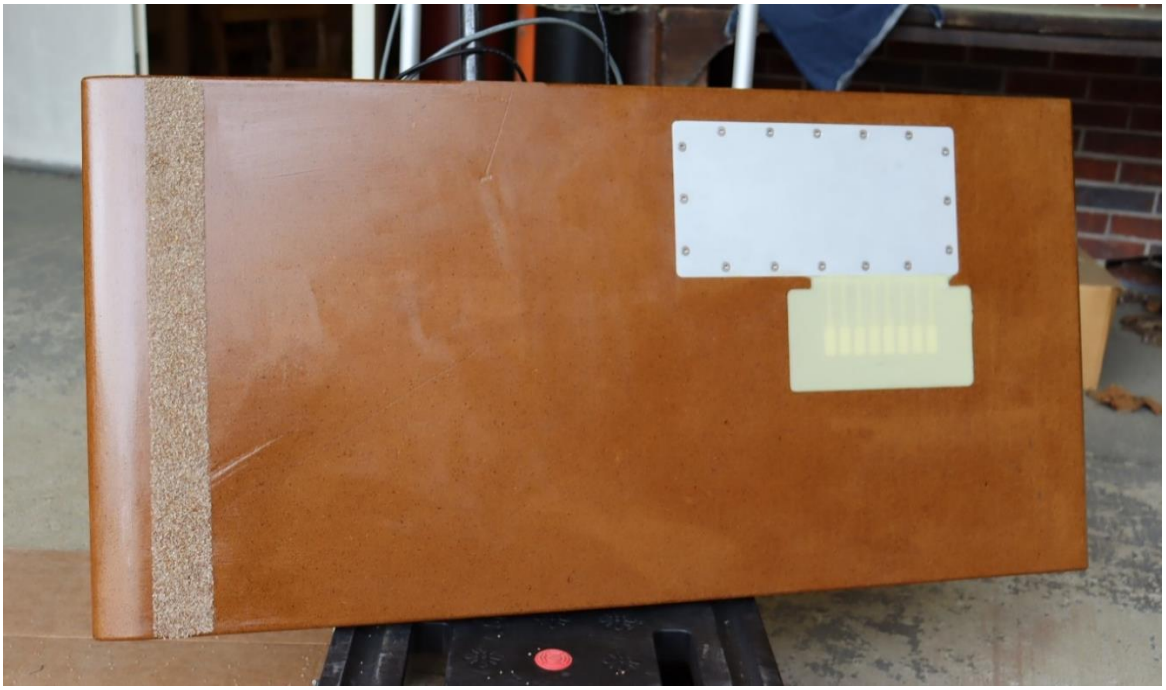

Figure 17 - Finished Fin with 8 hydrophone sensors

Figure 18 - Sensor Fin Hydrodynamic Profile

Figure 19 - Turbulence trip strip.

Figure 20 - Kayak with data collection system installed

Figure 21 - Installation of the fin

Figure 22 - Full system being towed

Data analysis

Overall, thirty-five data segments were identified for analysis while the array was towed in a total of three useful runs. Unfortunately, because of the difficulties encountered, tow speeds were limited to approximately two knots. During tow the following nominal signals were emitted one at a time by the controlled source for approximately thirty seconds: 50 Hz, 100 Hz, 200 Hz, 400 Hz, 800 Hz sinusoidal tones, broadband Gaussian random noise, and brief Gaussian pulses consisting of a sum of the above tones of 20 ms duration one second apart. Of course, propeller and motor noise from the tow craft were always present.

Presenting results from all thirty-five logged runs would be prohibitive, therefore results from a subset are provided in order to demonstrate comparative performance between the proposed processing approach and simple averaging over the hydrophone elements. An attempt has been made provide results that show the best performance and the worst performance. Another point is that the results are inherently qualitative (visual) since true acoustic signal values were not available. Finally, it is noted that the data were low-pass filtered and decimated to 4.8 kHz from the logged data rate of 48 kHz prior to any analysis.

All results are based on application of Equation (8) to the hydrophone data which is repeated here

$$\hat{y}_{s_k}(i\omega) = \frac{a^T S_{y^m}^{-1}(\omega) y_k^m(i\omega)}{a^T S_{y^m}^{-1}(\omega) a}.$$

The cross-spectral density matrix $S_{y_m}(\omega)$ was estimated using the well-known Welch's method with Hann windows of 4800 samples (1 s) and 50% overlap. The vector of measurements $y_k^m(i\omega)$ were just the retained values from each window used to estimate $S_{y_m}(\omega)$. As state before, a is just a vector of 1's. No

attempt was made to enhance the accuracy of the estimate by performing the non-linear approximate MMSE estimation algorithm. Furthermore, we did not develop the algorithm for time-domain estimation of anomalous acoustic transients.

Results are provided in Figure 23 through Figure 33; specifically time series from all eight channels, the spectrogram from one channel, the coherence between channel 0 and the other 7, the PSD's from all channels, the amplitude output of the GLS processor, and the amplitude output corresponding to straight averaging (the mean). Both methods produce a complex-valued output; however, for use in processing outputs from other compact arrays or sensor units to enable beamforming. Because of the high likelihood of multiple, somewhat coherent, sources (flow and/or sound) of pressure fluctuations impinging on the array at once, the coherence can vary. One set of results has been provided corresponding to each of the source cases described previously plus a case where no controlled sources was played. As is clearly observable, there are many harmonics visible in the data. Overall, every case demonstrates that the GLS-based processor provides at least some, albeit small sometimes, higher contrast of the signal as opposed to the nearby (in frequency) noise compared to straight averaging.

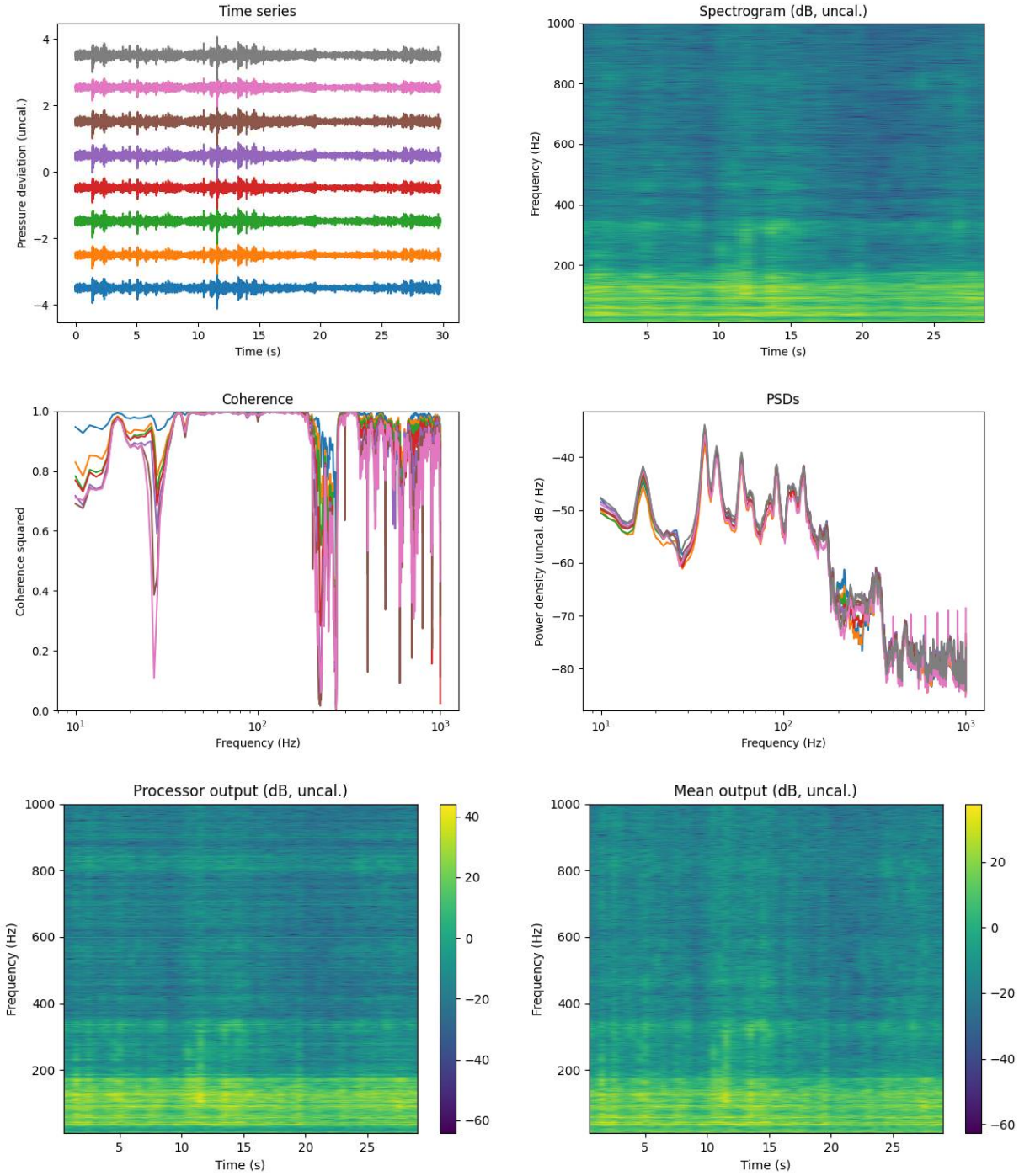

Figure 23. Results Run 3. No controlled acoustic source, nominal speed 2 knots. In this case the GLS processor was able to identify tones at 600 Hz and 900 Hz that are not in the mean output. See Figure 24 for a better view.

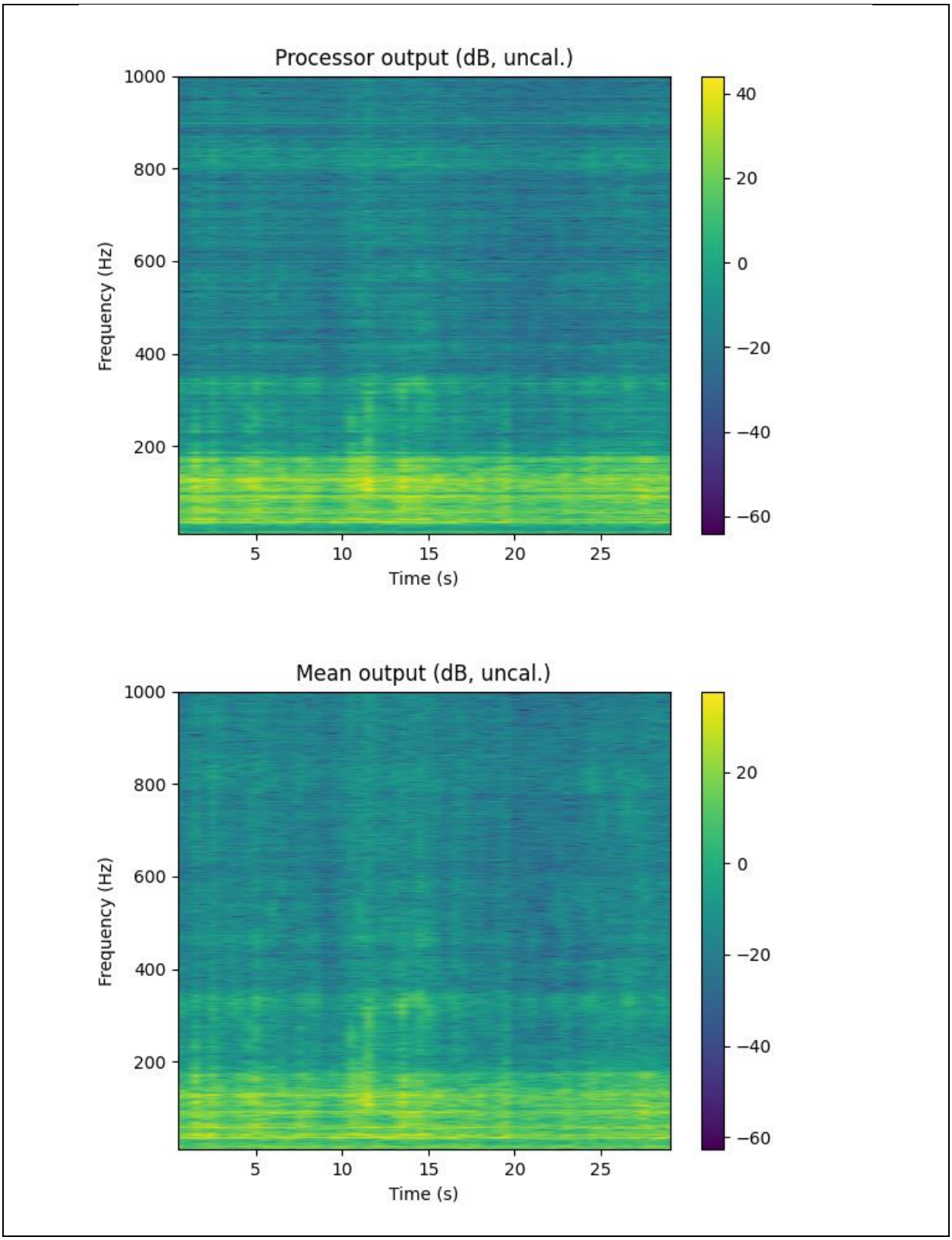

Figure 24. Enlarge processing outputs corresponding to Figure 23. Some tones are visible in the GLS processor output that are not visible in the mean output—especially at 600 Hz and 900 Hz.

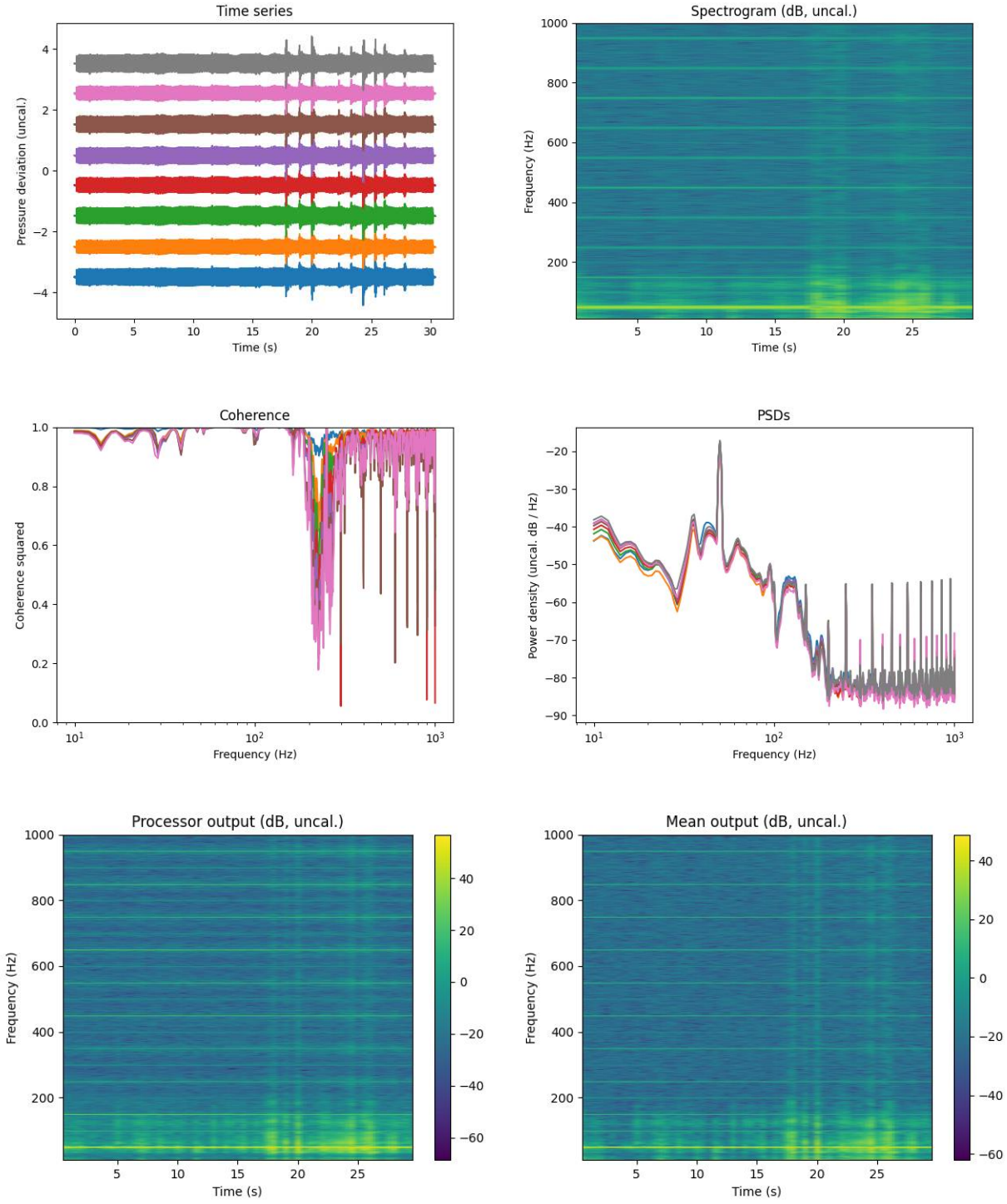

Figure 25. Results Run 2. 50 Hz primary tone, nominal speed 0 knots, but motor running. Notice the weak tones that are visible in the GLS processor output that are not in the mean output.

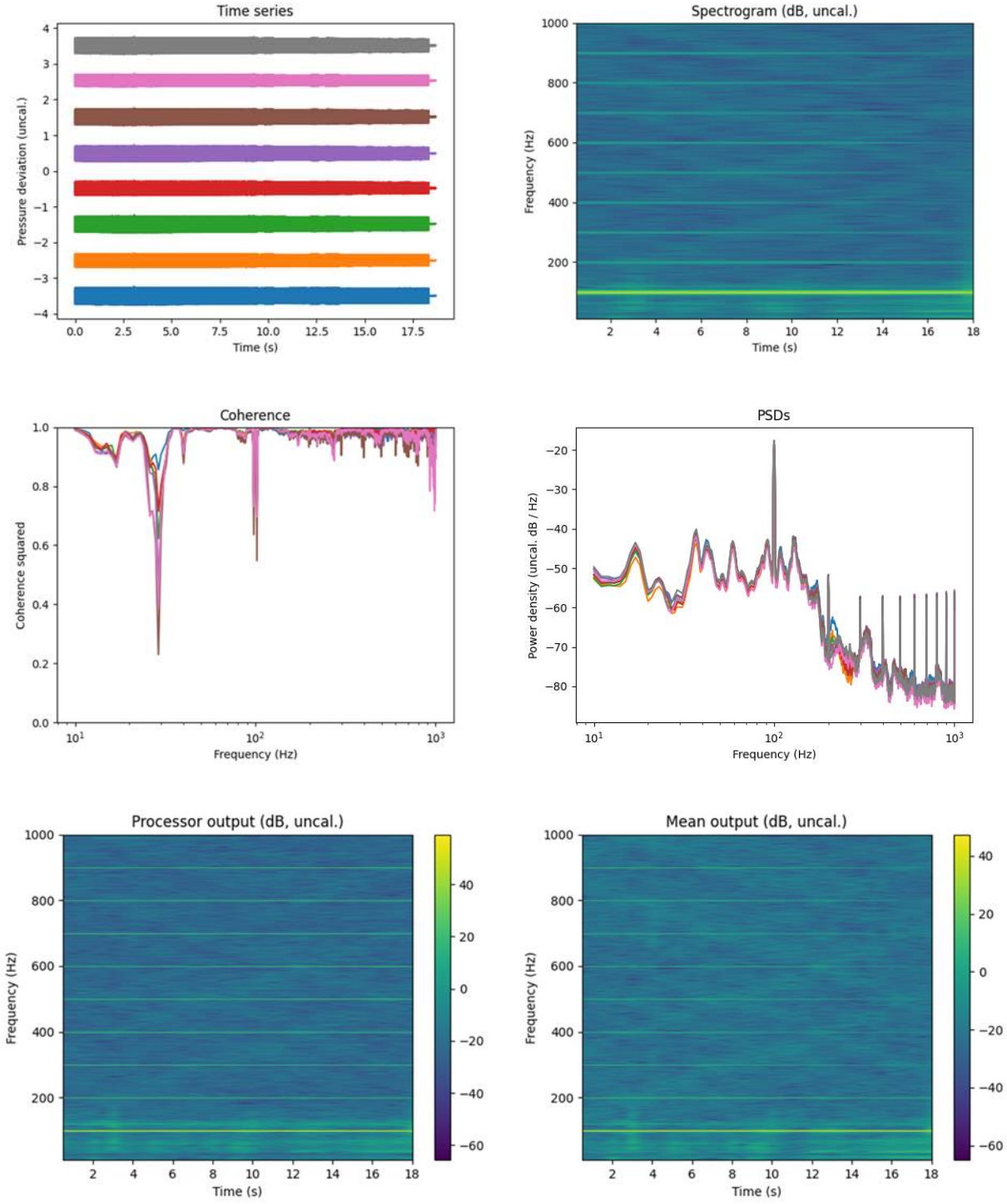

Figure 26. Results Run 3. 100 Hz primary tone, nominal speed 2.0 knots. In this case while the same tones are visible in both outputs, there are times when the mean output fades, but the GLS processor output does not.

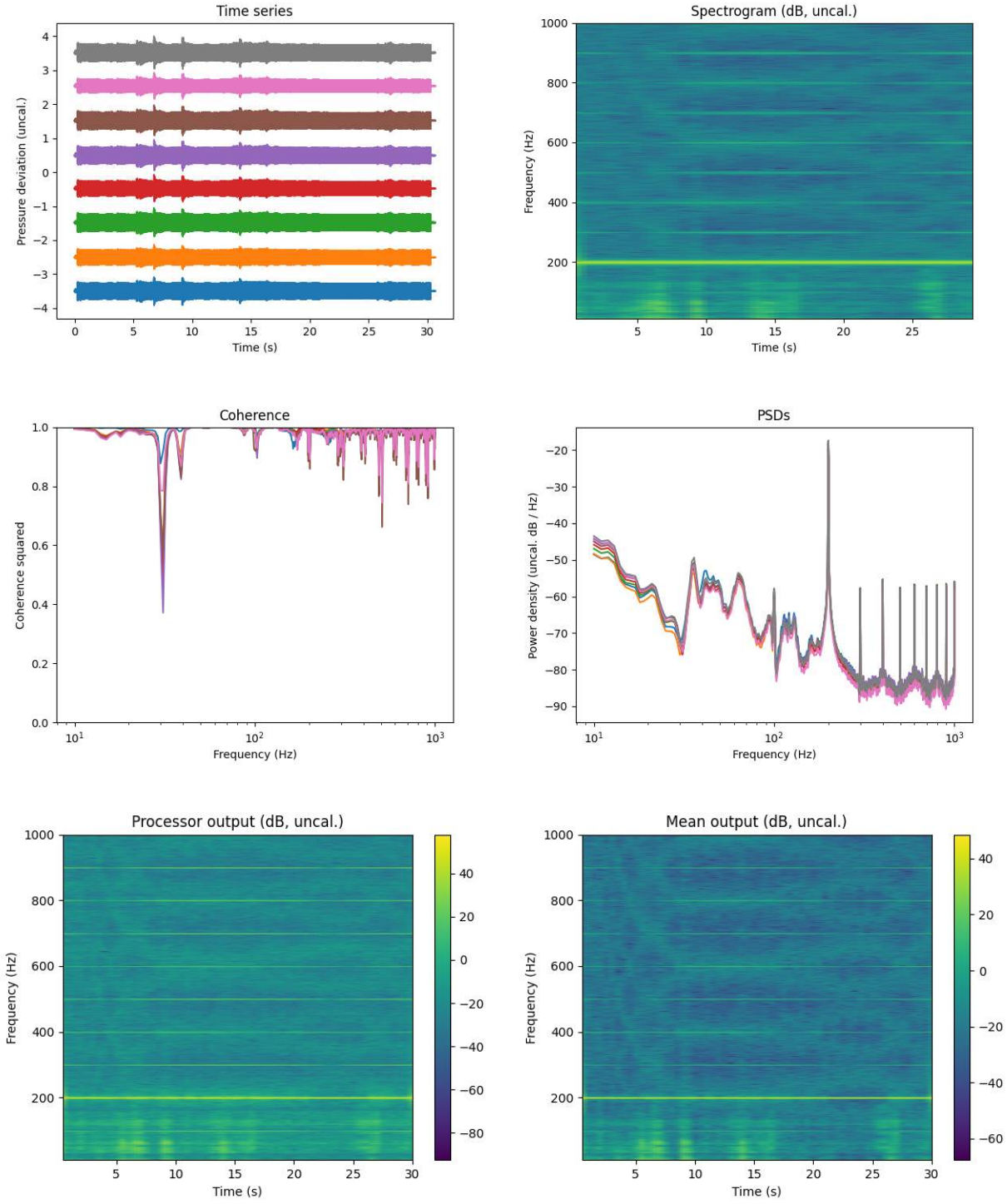

Figure 27. Results Run 2. 200 Hz primary tone, nominal speed 0 knots, motor running. Again, there are times when the mean output fades, but the GLS processor does not.

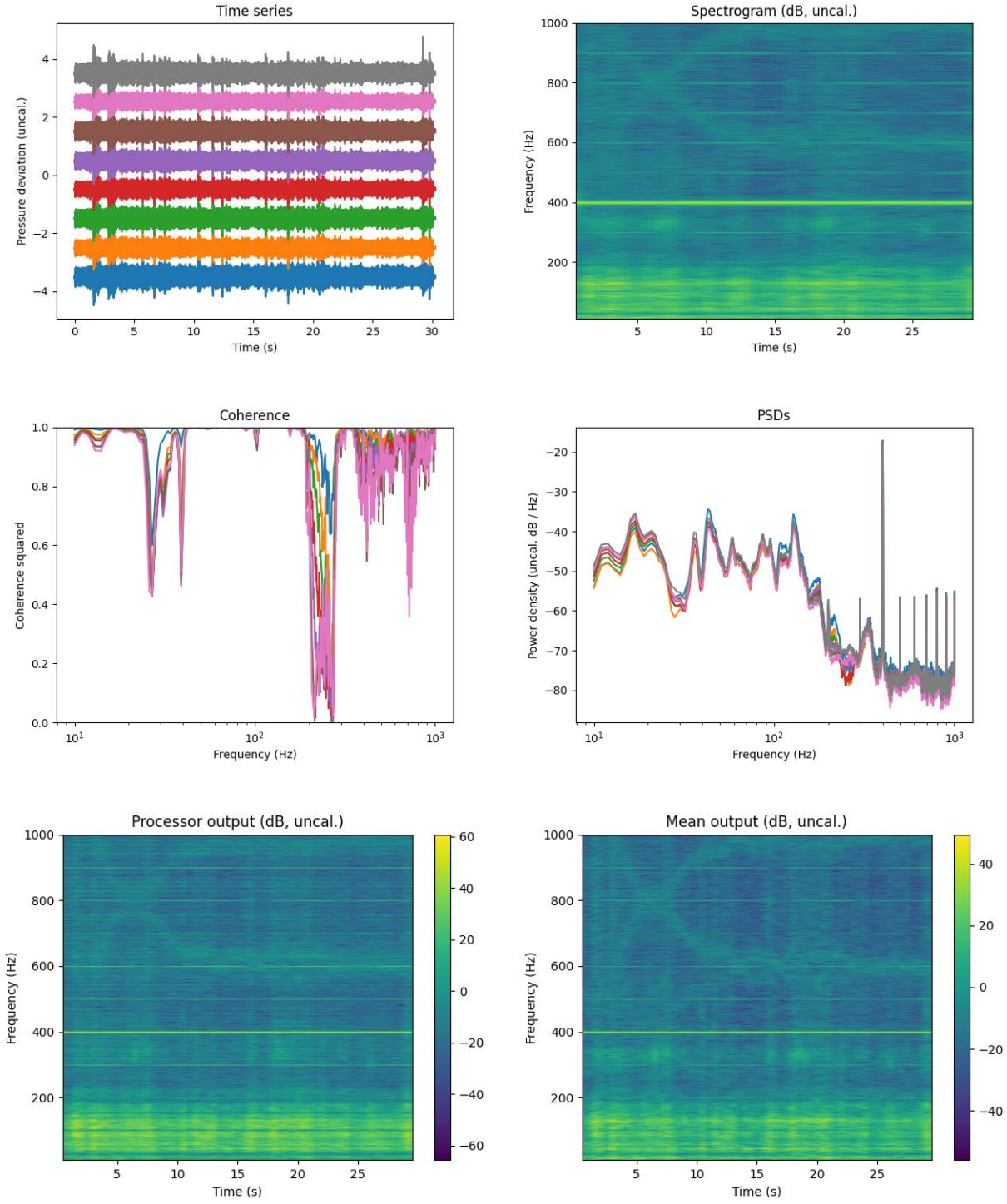

Figure 28. Results Run 1. 400 Hz primary tone, nominal speed 1.0 knots. There is more fading in the mean output than the GLS processor output, especially for the tone at 300 Hz.

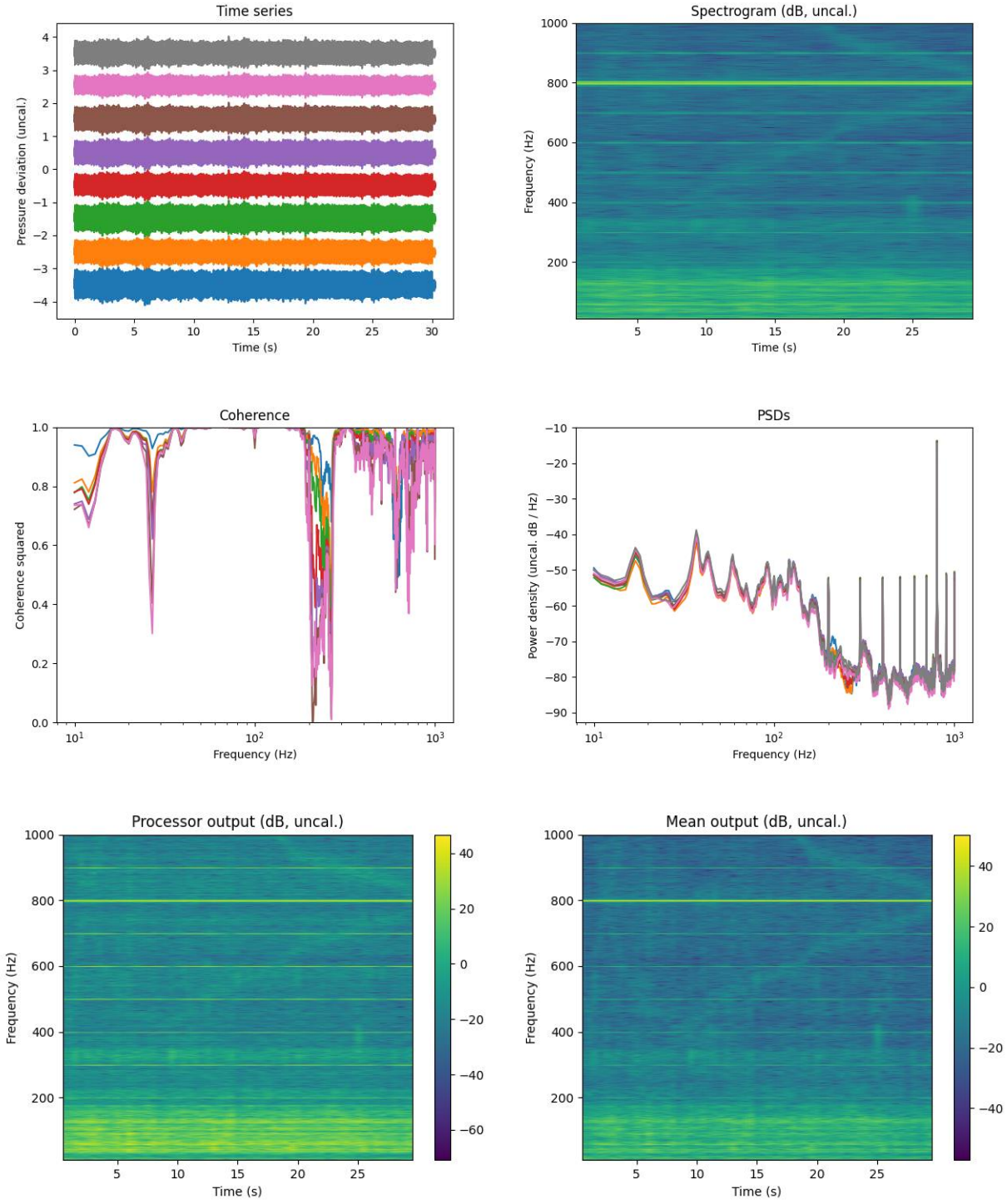

Figure 29. Results Run 3. 800 Hz primary tone, nominal speed 1.8 knots. Same comments as for the previous cases; however, in all fairness, it appears that the contrast for 900 Hz tone is about the same in both outputs.

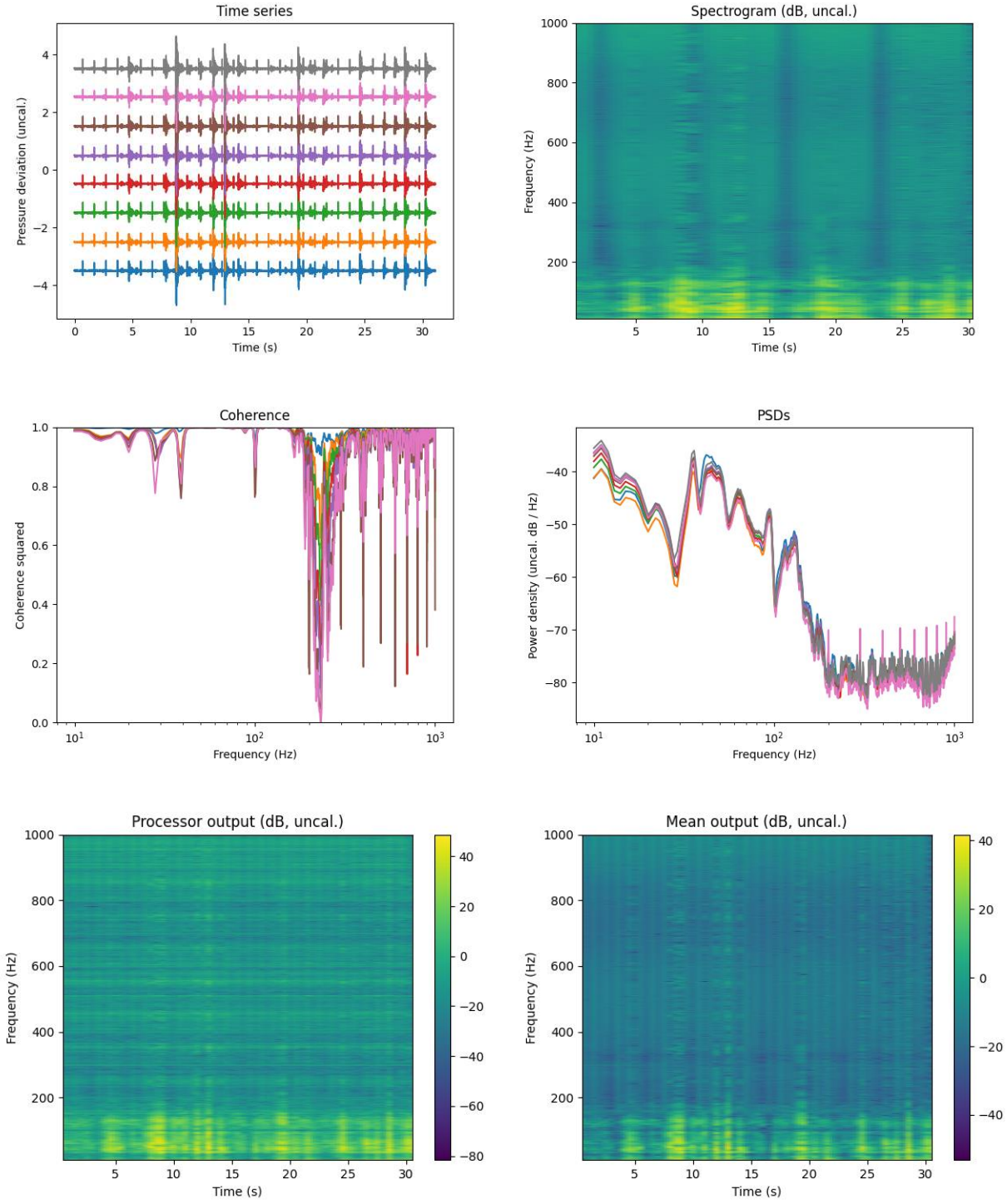

Figure 30. Results Run 2. Periodic pulses, nominal speed 0 knots, motor running. Better results from the GLS processor are not obvious at this resolution, but see Figure 31.

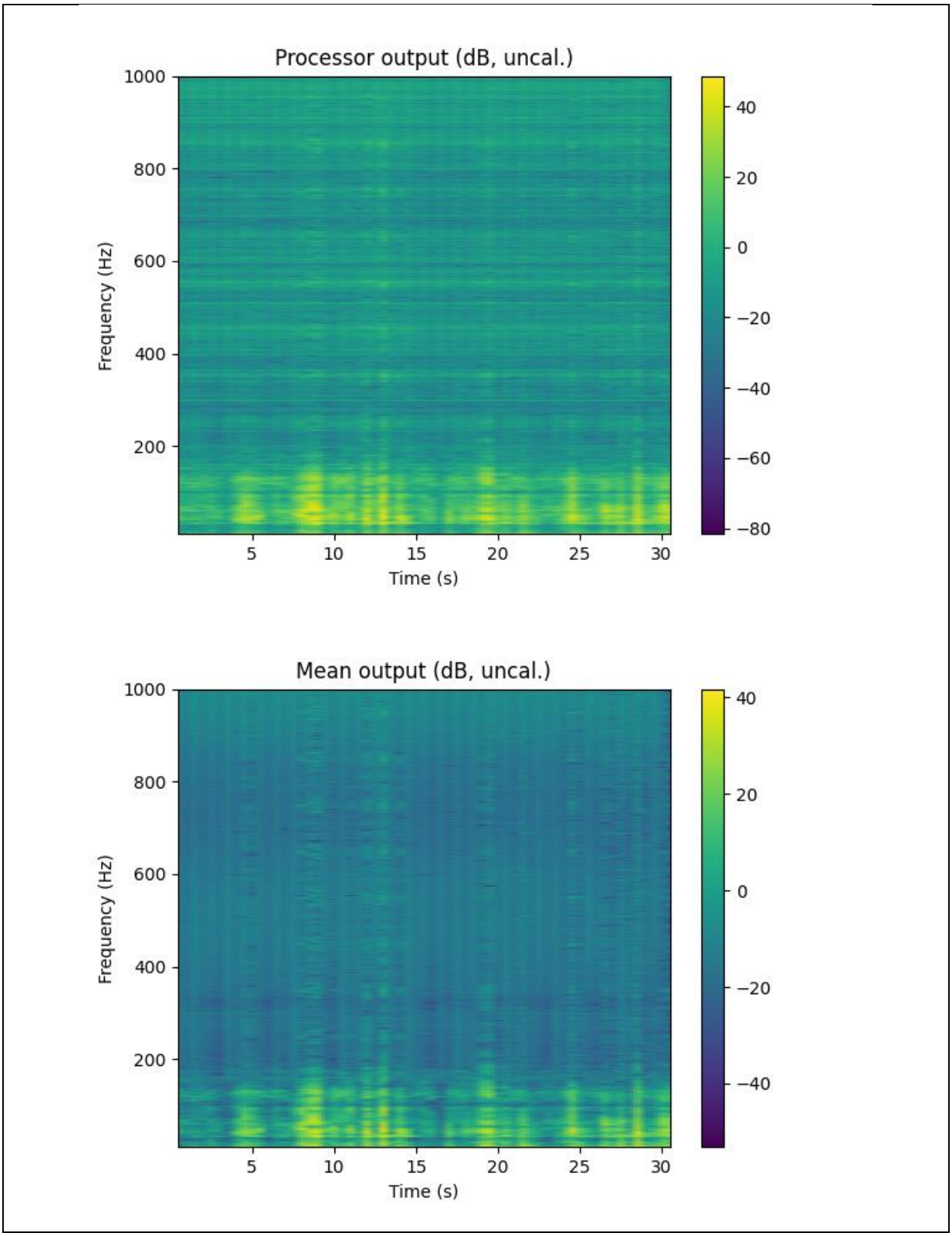

Figure 31. Enlarged processor outputs corresponding to Figure 30. Notice low-level narrow tones at 200, ~500 that are visible in the GLS processor output (very faint, but clearly there) are not in the mean output.

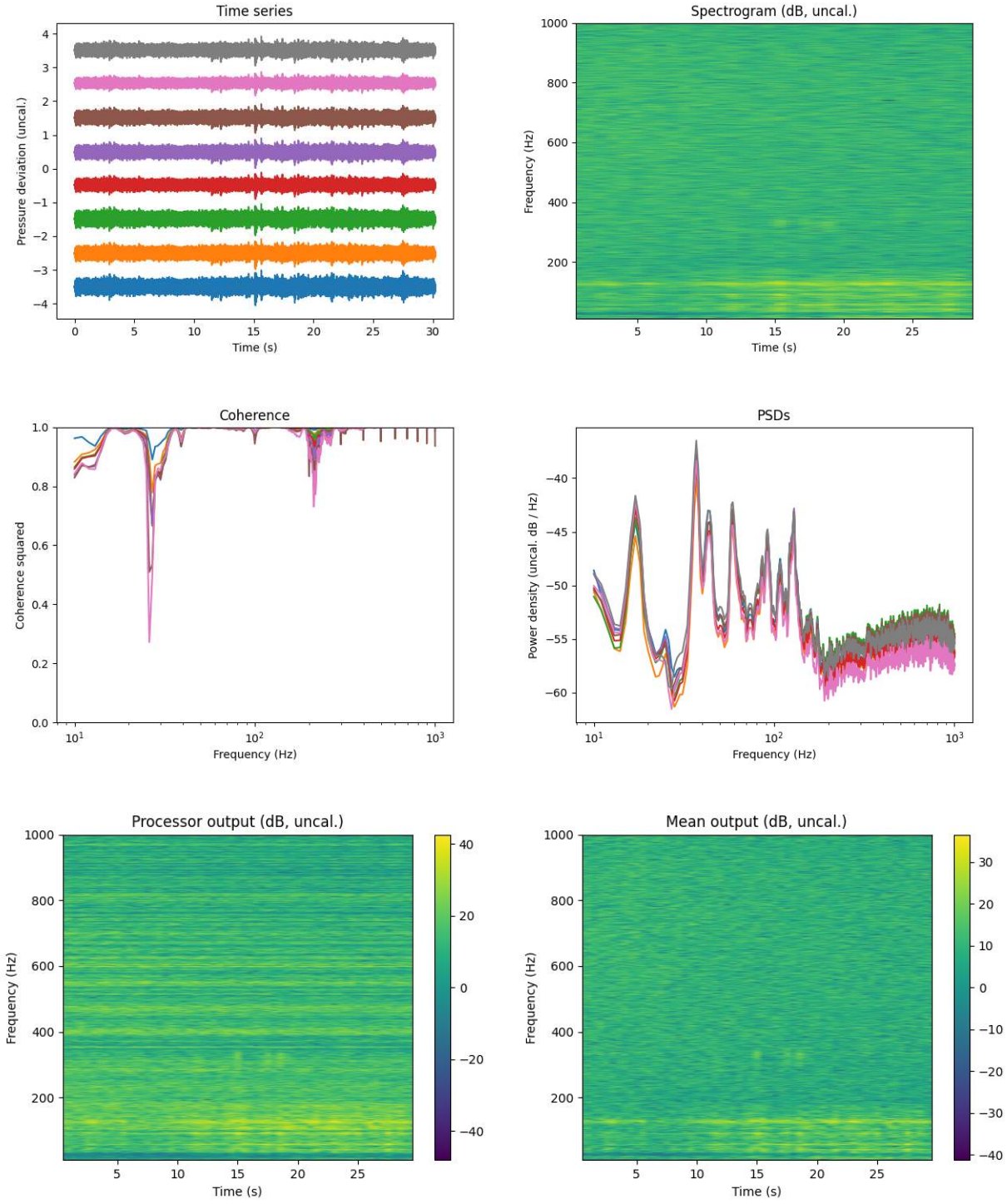

Figure 32. Results Run 3. Bandlimited white noise, nominal speed 1.8 knots. See Figure 33 for higher resolution images.

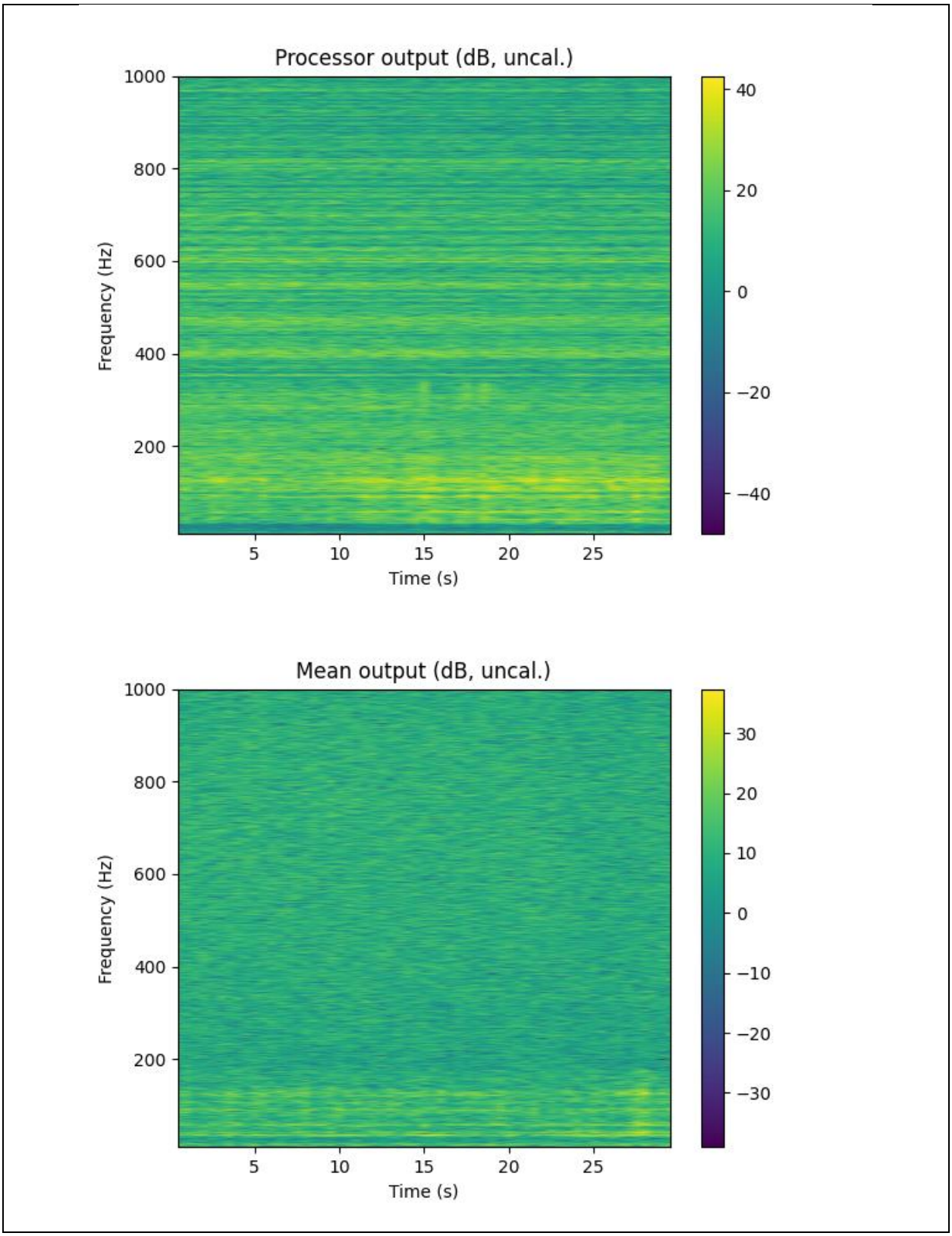

Figure 33. Enlarged processor outputs corresponding to Figure 32. Notice weak tone above 300 Hz can be seen in the GLS processor output, but not in the spectrogram nor the mean output.

Summary

A preliminary analysis of the potential performance of compact arrays of hydrophones has been presented. This reveals that performance gains in the case of minimum mean-squared error and generalized least-squared error processing are characterized by the compact array gain factor

$$G(\omega) = a^T C_n^{-1}(\omega) a,$$

where $a \in R^{N_c}$ is a vector of ones with length equal to the number of sensor elements in the compact array, and $C_n(\omega) \in C^{N_c \times N_c}$ is a coherence matrix of the flow noise. Thus, the gain factor can be more or less than the nominal array processing gain of N_c. Using a recently presented model [3] of the flow noise associate with turbulent wall-pressure fluctuations, this result was demonstrated.

Additionally, Monte Carlo simulations of the bearing-of-arrival estimation performance of an array system of five compact arrays was demonstrated using MUSIC as the bearing-of-arrival estimation algorithm in the case of two sources. These simulation results indicate consistently better performance for the compact array system, and in several cases, substantially better performance. Regardless of the underwater application, using a compact array with appropriate processing in place of a single hydrophone appears to have to the potential to provide significant processing gain and thus greater detection, estimation, and source characterization performance. While not demonstrated in this analysis, these ideas can be extended to detection of anomalous acoustic transients and active sonar applications with similar performance enhancements.

Furthermore, an underwater experiment was performed to validate the simulation results. A test apparatus was designed that contained a linear array of eight patch hydrophones spaced 15 mm apart center-to-center. This array was towed in a nearby freshwater lake while a range of acoustic source signals were played a few meters away. Unfortunately, the test apparatus had a stability issue that prevented towing in excess of two knots, but a sufficient amount usable data was collected.

All the analysis presented herein as well the remainder of the data analyzed revealed that using a processing scheme that exploits the *compact array hypothesis* as contrasted with simple averaging across the closely spaced patches provides more gain over flow noise—albeit the analyses were qualitative (visual) since we did not have a truth signal. Nevertheless, this is consistent with the analytical and numerical results that have been presented.

In conclusion, while the experiment did not proceed as planned, the results clearly indicate that exploiting the *compact array hypothesis* provides additional gain over flow noise and there is sufficient theoretical, numerical, and experimental evidence that this approach is viable for hydrophones similarly as it has been shown to be viable for compact arrays of microphones in atmospheric applications; where it is patented [8] by The University of Mississippi and is in commercial use. Ideally, opportunities to redesign and perform an experiment to assess performance at much higher speeds will be become available.

References

1. Fay, John F., “Optimum Flow Noise Cancelling Hydrophone Module,” U.S. Patent 4,388,711, 14 June, 1983.

2. Keith, William L.; Cipolla, Kimberly M.; and Williams, Michael R.; U.S. Patent 7,130,242 B1, 31 October 2006.
3. Frendi, Abdelkader and Man Zhang, "A New Turbulent Wall-Pressure Fluctuation Model for Fluid-Structure Interaction," Journal of Vibration and Acoustics, April 2020, Vol. 142, p. 021018-1 to 021018-9.
4. Goody, M. "Empirical Spectral Model for Surface Pressure Fluctuations," AIAA Journal, **42**(9), p. 1788-1794.
5. Hwang, Y.F., William K. Bonness, and Stephen A. Hambric, "Comparison of semi-empirical models for turbulent boundary layer wall pressure spectra," Journal of Sound and Vibration, 319 (2009), p. 199-216.
6. Ko, Sung H., "Performance of various shapes of hydrophones in the reduction of turbulent flow noise," Journal of the Acoustical Society of America, 93, (3), March 1993.
7. Ko, Sung H. and Schloemer, Howard H., "Flow noise reduction techniques for a planar array of hydrophones," Journal of the Acoustical Society of America, 92 (6), December 1992.
8. Frazier, William Garth, "Systems and methods for detecting transient acoustic signals," U.S. Patent 20,150,139,444 A1, May 2015.

REPORT DOCUMENTATION PAGE

1. REPORT DATE	2. REPORT TYPE	3. DATES COVERED	
		START DATE	END DATE
29 APR 2022	FINAL	1 JUN 2020	30 DEC 2021

4. TITLE AND SUBTITLE

Exploiting Hydrophone Flow Noise Spatiotemporal Correlation for Enhanced Signal Detection

5a. CONTRACT NUMBER	5b. GRANT NUMBER	5c. PROGRAM ELEMENT NUMBER
	N00014-20-1-2369	
5d. PROJECT NUMBER	**5e. TASK NUMBER**	**5f. WORK UNIT NUMBER**

6. AUTHOR(S)

GARTH FRAZIER

7. PERFORMING ORGANIZATION NAME(S) AND ADDRESS(ES)

UNIVERSITY OF MISSISSIPPI
113 FALKNER
UNIVERSITY MS 38677-9704

8. PERFORMING ORGANIZATION REPORT NUMBER

9. SPONSORING/MONITORING AGENCY NAME(S) AND ADDRESS(ES)

Office of Naval Research, OCEAN SENSING & SYSTEMS APPS DIV
875 N. Randolph Street, Suite 1425
Arlington, VA 22203-1995

10. SPONSOR/MONITOR'S ACRONYM(S)

11. SPONSOR/MONITOR'S REPORT NUMBER(S)

12. DISTRIBUTION/AVAILABILITY STATEMENT

Unlimited; Approved for Public Release

13. SUPPLEMENTARY NOTES

14. ABSTRACT

This report documents efforts to develop theory and experimental demonstration of the use of compact arrays of hydrophones for the purpose of reducing the effect of flow noise in undersea applications. Results indicate that in many circumstances, significant processing gain can be achieved over simple spatial averaging as achieved with flush-mounted patch hydrophones of equivalent cross-sectional area.

15. SUBJECT TERMS

Hydrophone, Compact array, Array processing, Signal processing

16. SECURITY CLASSIFICATION OF:			17. LIMITATION OF ABSTRACT	18. NUMBER OF PAGES
a. REPORT	b. ABSTRACT	C. THIS PAGE		
Unclassified	Unclassified	Unclassified	Unlimited	39

19a. NAME OF RESPONSIBLE PERSON	19b. PHONE NUMBER *(Include area code)*
William Garth Frazier	662-380-0234

PREVIOUS EDITION IS OBSOLETE.

STANDARD FORM 298 (REV. 5/2020)
Prescribed by ANSI Std. Z39.18